Pavement Data Analytics for Collected Sensor Data

October 2021

Final Report

U.S. Department of Transportation
Federal Aviation Administration

NOTICE

This document is disseminated under the sponsorship of the U.S. Department of Transportation in the interest of information exchange. The United States Government assumes no liability for the contents or use thereof. The United States Government does not endorse products or manufacturers. Trade or manufacturer's names appear herein solely because they are considered essential to the objective of this report. The findings and conclusions in this report are those of the author(s) and do not necessarily represent the views of the funding agency. This document does not constitute FAA policy. Consult the FAA sponsoring organization listed on the Technical Documentation page as to its use.

This report is available at the Federal Aviation Administration William J. Hughes Technical Center's Full-Text Technical Reports page: actlibrary.tc.faa.gov in Adobe Acrobat portable document format (PDF).

1. Report No. DOT/FAA/TC-21/34	2. Government Accession No.	3. Recipient's Catalog No.
4. Title and Subtitle PAVEMENT DATA ANALYTICS FOR COLLECTED SENSOR DATA		5. Report Date October 2021
		6. Performing Organization Code
7. Author(s) *Osman Erman Gungor, *Imad L Al-Qadi, **Navneet Garg		8. Performing Organization Report No.
9. Performing Organization Name and Address *Illinois Center for Transportation Department of Civil and Environmental Engineering University of Illinois at Urbana–Champaign 205 North Mathews Avenue, MC-250 Urbana, IL 61801		10. Work Unit No. (TRAIS)
12. Sponsoring Agency Name and Address **Federal Aviation Administration William J. Hughes Technical Center Aviation Research Division Airport Technology R&D Branch Atlantic City International Airport, NJ 08405		13. Type of Report and Period Covered Final Report
		14. Sponsoring Agency Code ANG-E262
15. Supplementary Notes Conducted in cooperation with the Federal Aviation Administration.		

16. Abstract

The Federal Aviation Administration instrumented four concrete slabs of a taxiway at the John F. Kennedy International Airport to collect pavement responses under aircraft and environmental loading. The study started with developing preprocessing scripts to organize, structure, and clean the collected data. As a result of the preprocessing step, the data became easier and more intuitive for pavement engineers and researchers to transform and process. After the data were cleaned and organized, they were used to develop two prediction models. The first prediction model employs a Bayesian calibration framework to estimate the unknown material parameters of the concrete pavement. Additionally, the posterior distributions resulting from the calibration process served as a sensitivity analysis by reporting the significance of each parameter for temperature distribution. The second prediction model utilized a machine-learning (ML) algorithm to predict pavement responses under aircraft and environmental loadings. The results demonstrated that ML can predict the responses with high accuracy at a low computational cost. This project highlighted the potential of using ML for future pavement design guidelines as more instrumentation data from future projects are collected to incorporate various material properties and pavement structures.

| 17. Key Words

Airfield pavement data analytics, Machine learning, Bayesian calibration, Sensor data | 18. Distribution Statement
This document is available to the U.S. public through the National Technical Information Service (NTIS), Springfield, Virginia 22161. This document is also available from the Federal Aviation Administration William J. Hughes Technical Center at actlibrary.tc.faa.gov. | |
| 19. Security Classif. (of this report)
Unclassified | 20. Security Classif. (of this page)
Unclassified | 21. No. of Pages
49 | 22. Price |

Form DOT F 1700.7 (8-72)   Reproduction of completed page authorized

ACKNOWLEDGEMENTS

TABLE OF CONTENTS

LIST OF FIGURES

LIST OF TABLES

LIST OF SYMBOLS AND ACRONYMS

AC	Asphalt concrete
CMS	Climate-materials structure
CRREL	Cold Regions and Research and Engineering Laboratory
DAS	Data-acquisition system
DOE	Design of experiment
EICM	Enhanced integrated climatic model
FAA	Federal Aviation Administration
F.B.	A sensor that did not collect any data from the beginning
FE	Finite element
ICT	Illinois Center for Transportation
ID	Infiltration drainage
JFK	John F. Kennedy International Airport
MAP	Maximum a posteriori
MCMC	Markov chain Monte Carlo
MD	McDonnell Douglas
ML	Machine learning
MSE	Mean square error
NA	Not available
NCHRP	National Cooperative Highway Research Program
NR	No response
R^2	Coefficient of determination
RMSE	Root mean square error
SVM	Support-vector machine
T.E.	A sensor that collected data with no anomalies until the end

EXECUTIVE SUMMARY

The Federal Aviation Administration (FAA) instrumented four concrete slabs of a taxiway at the John F. Kennedy International Airport (JFK) to collect pavement responses under aircraft and environmental loadings. Two types of data were collected: (1) static data to study curling in slabs (wet-freeze climatic region) and (2) dynamic data to study load-induced strain in slabs under multi-gear aircraft such as Airbus (A)380, Boeing-777, or Boeing-747.

The collected data were provided to the research team in a file format that could be visualized and processed only by using HBM's InField field performance and analysis software. The research team developed preprocessing scripts that could transform the data into two file formats: Microsoft® Excel® and SQLite. This transformation inherently structured the data, which became more intuitive for pavement researchers and engineers to use. Additionally, malfunctioned sensors were identified and data were cleaned by detecting and removing anomalies. Approximately 250 aircraft images were analyzed to extract the type and model of aircraft that produced the sensor measurements. The preprocessing step also included the development of a signal-processing algorithm that processed and compressed the signals under aircraft loading and extracted the peak responses.

The collected data were used to develop two prediction models. The first model employed a Bayesian calibration framework to estimate the unknown material properties of concrete pavement slabs. The enhanced integrated climatic model (EICM) was used to produce temperature profiles based on meteorological inputs such as air temperature and humidity. The calibration framework searched for the material parameters that matched EICM's calculations with field-temperature measurements. In addition to finding calibrated values for the material properties, the Bayesian calibration also produced the posterior distribution for each of the parameters. These posterior distributions served as a sensitivity analysis by reporting the significance of each parameter for temperature distribution.

In addition, a model was developed to estimate pavement responses using the low-cost computation machine-learning (ML) algorithms developed as a surrogate to the finite element mechanistic approach. Both static and dynamic responses were predicted based on climatic data using a support-vector machine, one of the most commonly used ML algorithms. Explanatory variable analysis for ML development demonstrated the capability of ML approaches to consider variables omitted by mechanistic approaches, while providing prediction with high accuracy and low computational cost.

For similar projects in the future, the research team recommends utilizing a design of experiment (DOE) in the data collection process. The DOE would lead to more comprehensive data sets that can cover all important aircraft types and climatic conditions in a more balanced and systematic way. Such comprehensive and balanced data sets can improve the generalizability of pavement data analytics and the performance of prediction models. It is suggested to incorporate two more variables into the database: wander and speed. In particular, the lateral position of aircraft with respect to the location of sensors (i.e., wander) is expected to have a significant impact on the extraction of peak responses and the accuracy of prediction models.

1. INTRODUCTION

The Federal Aviation Administration (FAA) has been proactively involved in many projects to advance pavement design, analysis, and rehabilitation procedures. In one project, four concrete slabs of a taxiway at John F. Kennedy International Airport (JFK) were instrumented to collect the pavement response under aircraft and environmental loading. Two types of data were collected: static data (pavement response to environmental loading) and dynamic data (pavement response to dynamic loading).

Each pavement slab of the taxiway has 20-in.-thick concrete supported by two base layers. The first base layer is a 4-in.-thick, asphalt concrete (AC)-modified base; the second base layer is a 6-in.-thick, dense-graded granular base. The cross section of the instrumented taxiway is presented in figure 1.
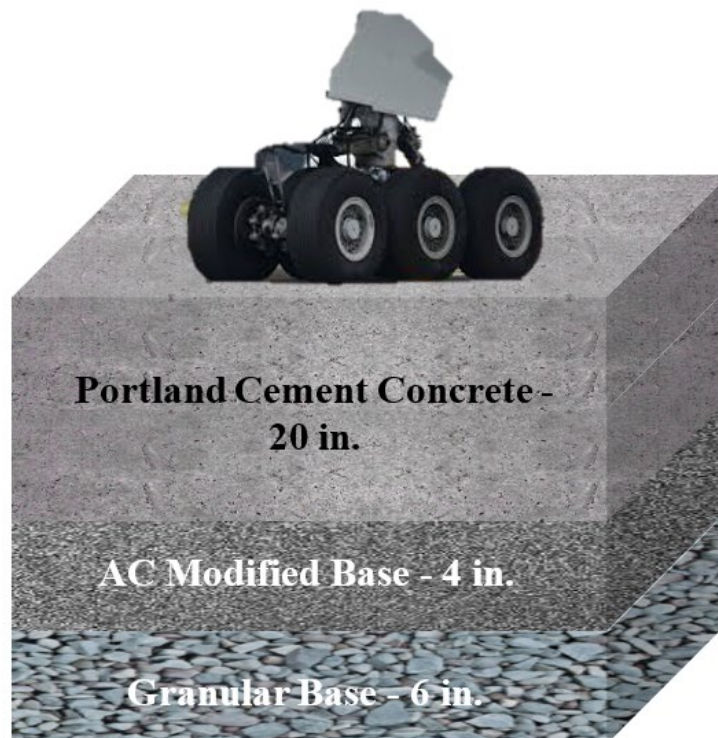
Figure 1. Cross Section of the Instrumented Taxiway (AC = Asphalt Concrete)

In total, 40 strain gauges, 8 pressure cells, and 6 thermocouples were installed. The instrumentation layout is given in figure 2. While the strain gauges labeled A were instrumented at the mid-depth of the slab, strain gauges labeled B were instrumented at the bottom of the slab. Furthermore, the temperature gauges were placed at three different depths: 10, 16, and 19 in. Also, pressure cells were embedded at the interface between the concrete slab and the asphalt-modified base.
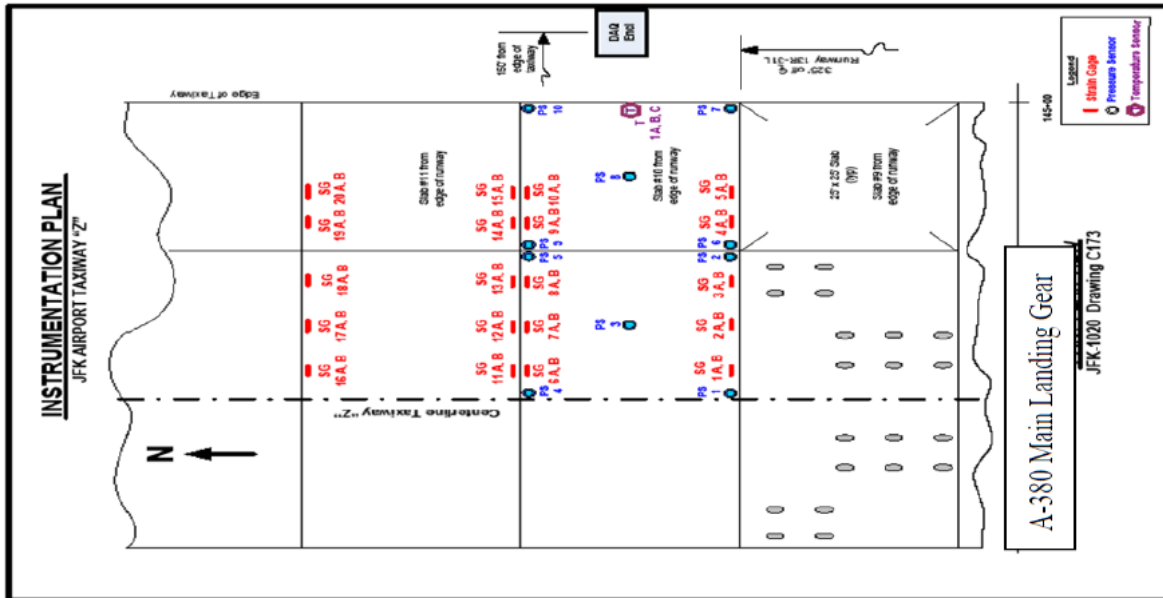
Figure 2. Instrumentation Layout

2. DATA PREPROCESSING

The collected sensor data was provided in a format that could be visualized and processed only by using the software program HBM's InField field performance and analysis software. However, this software is not designed for data analysis. The raw data needed to be extracted to transfer them to more versatile environments (e.g., Microsoft® Excel® or SQLite) and restructure them to make them intuitive for researchers and engineers to use.

Data preprocessing was performed by developing two scripts. The first script was developed using AutoHotkey, an open-source scripting language for Microsoft® Windows®, which allowed automating mouse and keyboard inputs. The script was used to emulate the human behavior of opening the Infield software, uploading the sensor data, and copying and pasting it to Excel files, along with the metadata, which was important for extracting the date and time of data collection. Because InField was crashing with attempts to copy data greater than some certain limit, the data had to be extracted in smaller groups (i.e., Excel files). The second script, which was developed using MATLAB, was employed to go through these small Excel files and merge them into a single file. After the Excel files were generated, they were also transferred to SQLite databases. Sections 2.1 and 2.2 explain how the databases were organized in both Excel and SQLite formats.

2.1 STATIC-DATA FILE ORGANIZATION

Static data were collected hourly at the beginning of each hour for 5 seconds (s) at 5 Hz when the pavement was not loaded by aircraft. The FAA provided 70 data files, which were compatible with InField. These files were organized and regrouped into 10 Excel and SQLite files, depending on the month of the year when the data were collected (e.g., April 2011 or July 2012). Four sheets that store information about the data collection process were inserted into each of the 10 Excel (or

2

SQLite) files. These sheets are called *meta-sheets*, because they store metadata. Table 1 provides the names of these four meta-sheets, along with their descriptions.

Table 1. Names of Meta-Sheets and Their Descriptions

Meta-Sheet Name	Description	Illustrative Data
Initial_Date_Time	Initial date and time of data collection at their corresponding time zone	2011_4_16_10_Eastern (yy_mm_dd_hh_Time_Zone)
End_Date_Time	End date and time of data collection at their corresponding time zone	2011_4_16_10_Eastern (yy_mm_dd_hh_Time_Zone)
Gaps_in_Data	Starting and ending date and time of the gaps in data	None
Missing_Sensors	Missing sensor names	SG_1B, SG_2B

In addition to the four meta-sheets, there are other pages that keep the sensors' data. The naming convention of these pages is in the format YY_MM_DD_HH_Time Zone, so the names can be parsed to extract the date and time of the data collection, along with the time zone.

2.2 DYNAMIC-DATA FILE ORGANIZATION

Unlike the static data, dynamic data were not collected continuously. The dynamic data were collected only when a plane was passing the instrumented slabs. Photographs of planes were taken to extract the model and gear configuration of the plane applying the load.

There were approximately 75 data files in ".sie" format, which can be processed only by using Infield. These files were transferred to Excel and SQLite files by using the similar scripts explained in section 2.1. Each file (SQLite or Excel) has the data from five to nine runs (i.e., airplanes).

The name of each data file includes the day that the dynamic data were collected. Each data file has multiple sheets (i.e., runs) that store the data collected by sensors under an aircraft loading. The name of each sheet refers to the date and time of data collection (YY_MM_DD_HH_MM_Time Zone). Additionally, each file has a sheet titled "missing_sensors," which lists the sensors not working on the day of data collection.

3. DATA EXPLORATION

3.1 STATIC DATA

As shown in table 1, each data file has its own initial and end day and time. However, data collection was interrupted between initial and end dates because of various technical issues, such as solar-energy interruption due to weather conditions. Table 2 summarizes the static data by reporting the number of data points, the number of missing hours, and initial and end dates for the data collection.

Table 2. Static Data Summary

Initial Date	Initial Time	End Date	End Time	Missing Sensors	Number of Data Points	Number of Missing Hours
15-Apr-11	16:00	25-Apr-11	12:00	None	256	5
4-May-11	13:00	27-May-11	7:00	None	269	278
3-Jan-12	13:00	1-Feb-12	18:00	9 strain gauges	542	160
1-Feb-12	20:00	21-Feb-12	19:00	9 strain gauges and 6 temperature sensors	467	13
6-Mar-12	12:00	25-Mar-12	9:00	9 strain gauges	282	172
2-Apr-12	9:00	22-May-12	20:00	9 strain gauges	940	272
13-Jul-12	8:00	31-Jul-12	8:00	9 strain gauges	375	57
13-Aug-12	7:00	11-Sep-12	9:00	9 strain gauges	535	163
5-Dec-12	14:00	2-Jan-13	12:00	9 strain gauges	666	5
31-Jan-13	15:00	3-Feb-13	13:00	9 strain gauges	71	0

As mentioned, static data were collected hourly at the beginning of each hour for 5 s at 5 Hz. In other words, approximately 25 data points were collected for each hour. These data points, as expected, showed very little variance within 5 s because there was no loading. Therefore, their mean was calculated and considered as the data point that corresponds to a particular hour, so that the variation of measurements with respect to time could be analyzed. Figure 3 shows an example of the data collected by a thermocouple near the bottom of a slab.
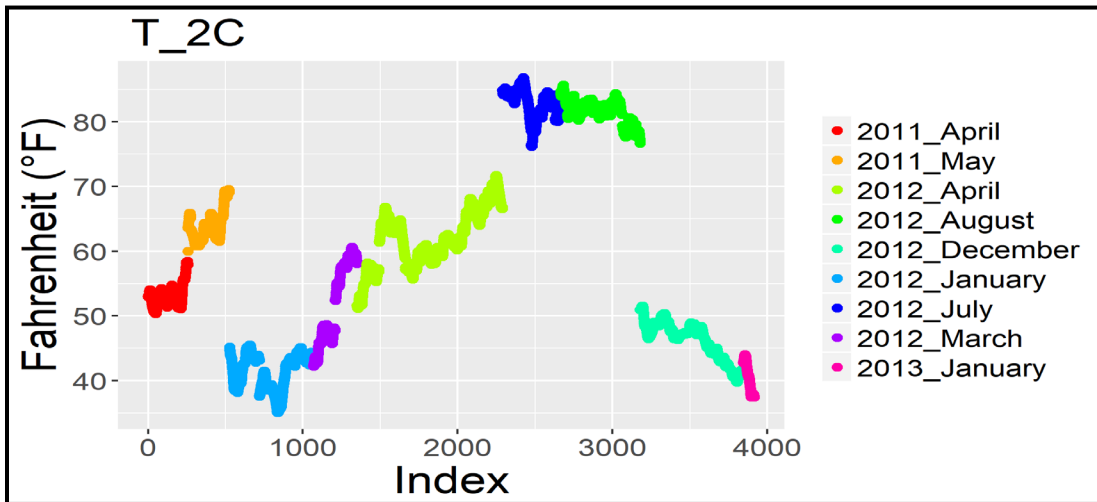
Figure 3. Example of Temperature Data Near the Bottom of a Slab

Although thermocouples managed to collect data throughout the analysis period, some anomalies were observed in strain-gauge measurements. Figure 4 (a and b) shows the strain measurements with respect to time for the gauges SG_6A and SG_15B, respectively. As shown, after January 2012, the gauges started exhibiting anomalies. Similarly, other gauges showed the same behavior. The plots for all the sensors are given in appendix A.
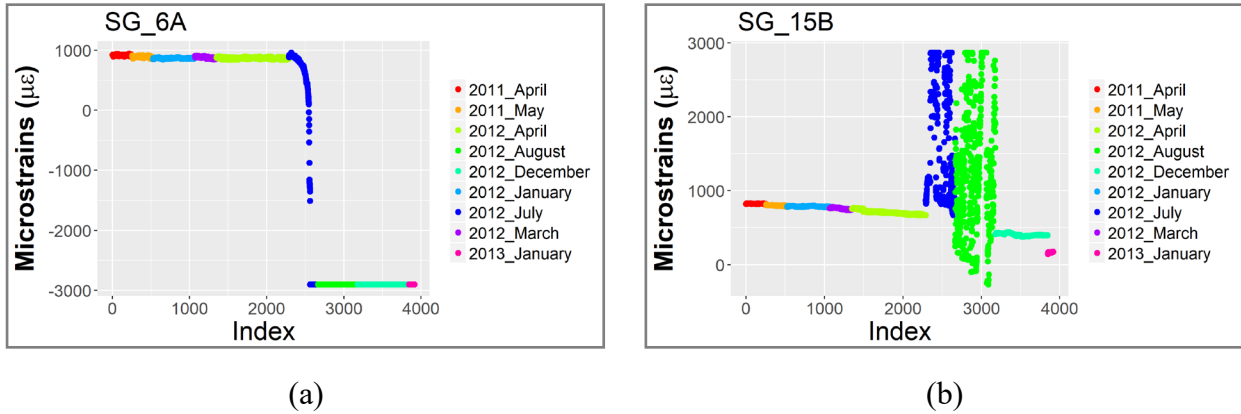
Figure 4. Anomalies for Strain Gauges SG_6A (a) and SG_15B (b)

Table 3 shows the month and year when sensors started exhibiting anomalies. In table 3, T.E. indicates a sensor that collected data with no anomalies from beginning to end; F.B. indicates a sensor that did not collect any data from the beginning.

Table 3. Sensors and Their Failure Dates

Sensor Name	Failure Date
SG_1B	T.E.
SG_2B	T.E.
SG_3B	January 2012
SG_4B	July 2011
SG_5B	F.B.
SG_6B	T.E.
SG_7B	F.B.
SG_8B	January 2012
SG_9B	July 2011
SG_10B	June 2011
SG_11B	T.E.
SG_12B	June 2011
SG_13B	F.B.
SG_14B	F.B.
SG_15B	T.E.
SG_16B	January 2012
SG_17B	T.E.
SG_18B	August 2011
SG_19B	T.E.
SG_20B	F.B.

3.2 DYNAMIC DATA

The dynamic data were collected under various aircraft loadings. Aircraft identification was based on photographs captured by a camera mounted on the data-acquisition system (DAS) cabinet. For

some images, the frame did not capture entire body of aircrafts due to mistiming of the shot. Such images could not be used to identify the type of aircraft (figure 5).

Figure 5. Example of an Image That Lacks Enough Information to Identify the Aircraft

An algorithm that consists of a set of rules was developed to identify aircraft from captured images. Because the majority of aircraft is either Airbus or Boeing, details about identifying other aircraft, such as the McDonnell Douglas DC-10 (MD-10), are omitted herein. The steps of the framework are listed below:

1. Check the position of the engine:

   a. If the engine is located by the fin (i.e., vertical stabilizer), it cannot be an Airbus or a Boeing. Please note that some models of Bombardier or McDonnell Douglas also do not have an engine by the fin. However, those aircraft can easily be differentiated from a Boeing 737 and Airbus A320 by their characteristic features, such as a very pointed nose or the rectangular rear ending.

   b. If the engine is not located by the fin, go the Step 2.

2. Check the type and number of gears:

   a. If an aircraft has two single gears, it is either a Boeing 737 or an Airbus A320. For further classification, go to step 4.

   b. If an aircraft has two tandem gears, it is either a Boeing 757, a Boeing 767, Boeing 787, Airbus A350 or an Airbus A330. For further classification, go to step 5.

   c. If an aircraft has two tridem gears, it is a Boeing 777.

   d. If an aircraft has two tandem gears and a single gear, it is an Airbus A340.

   e. If an aircraft has two tandem gears and two tridem gears, it is an Airbus A380.

   f. If an aircraft has four tandem gears, it is a Boeing 747.

3.   If the type of aircraft could not be identified in Step 2, proceed to step 4.

4.   If the candidate aircraft is determined to be a Boeing 737 or an Airbus A320 (Step 2a):

    a.   If the aircraft has a dorsal fin, it is a Boeing 737.

    b.   If the aircraft does not have a dorsal fin and has four doors in total (and two of these doors in the middle are next to each other), it is an Airbus A320.

    c.   If the aircraft does not have a dorsal fin, has four doors in total, and none of the doors are adjacent to another, it is an Airbus A321.

    d.   If the aircraft does not have a dorsal fin and has three doors, it is an Airbus A319.

5.   If the aircraft is determined to be a Boeing 757, a Boeing 767, Boeing 787, Airbus A350, or an Airbus A330 (Step 2b):

    a.   If the bottom of the cockpit windows is not V-shaped, it is an Airbus A330. This is the main visual difference between Airbus and Boeing intermediate- and small-sized aircraft. Please note that there was no picture for Airbus A350, therefore we could not develop any rule for this model.

    b.   If the corner cockpit window has five edges, it is Boeing 787.

    c.   The diameter of the body of Boeing 767 is much larger than that of a Boeing 757. Also, door and passenger configurations are different between these two aircraft models.

6.   At this stage, the aircraft model is either identified, or the candidate aircraft-type identification is reduced to a few models. In this step, the fleet of the airlines should be found online and compared with the candidate aircraft types. Generally, the comparison results in identifying the aircraft type.

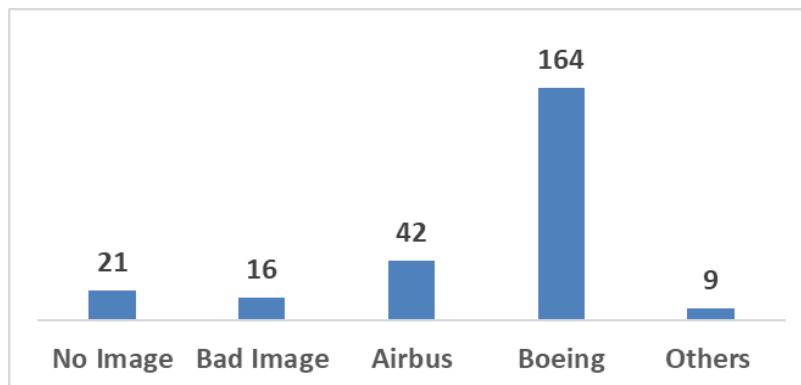The overall result of aircraft image distributions is given in figure 6.

Figure 6. Overall Aircraft Distribution

The aircraft model distribution within Airbus and Boeing is given in figure 7. The aircraft models on the x-axis are ranked based on their size, ranging from small to large. It should be noted that almost all models have a couple of different versions. In this study, all versions are grouped under the name of the model. For example, Boeing 777-200 and Boeing 777-200ER are grouped under Boeing 777.
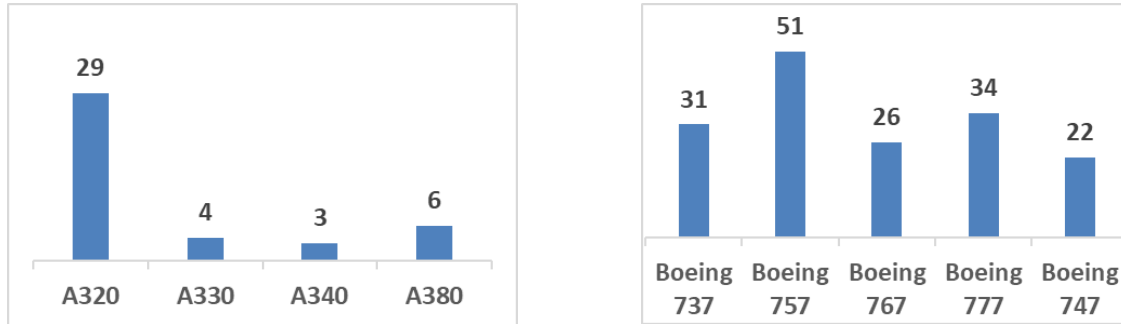

Figure 7. Aircraft Model Distribution Within Airbus and Boeing Fleets

3.3 SIGNAL PROCESSING

Collected dynamic data can be interpreted as a signal that is essentially a time-series showing variation when a plane travels over the sensors. With that interpretation, it was required to develop signal-processing algorithms to extract the responses to each airplane. Literature suggests that such signal-processing algorithms have been developed and used in many pavement-instrumentation projects.

In this study, there was a unique challenge in development of signal-processing algorithms. Two variables, speed and wander (i.e., lateral position of vehicles with respect to the sensors), that simplify extracting the peak responses were unknown. However, these variables were generally known and controlled in other studies. A signal-processing framework that addresses these challenges is outlined in the following sections of the report. It should be noted that the framework not only extracts peak responses but also trims the part of the signal that does not carry information. As a result of this trimming, the size of the signal is reduced, thus leading to a reduction in data storage.

3.3.1 Signal Filtering

Noise reduction in the signal was an issue in the development of the signal-processing framework. Generally, as suggested by subject matter literature, low-pass filters, such as the moving average, have been used to address this issue. However, for this study, these filters did not work well, as they may cause a loss of information by trimming the "peaks" of the signal. For example, when a gear passes over sensors, the signal appears as a spike, which can be masked by an averaging filter.

This study employed a technique called "Savitzky-Golay" (Orfanidis, 1995). This filtering technique outperforms conventional averaging filters by preserving the high-frequency component of the signals. It essentially fits the user-defined degree of polynomial to the part of the data

extracted by a sliding window. The length of the window is also user defined. The degree of polynomial and the window length were selected as 2 and 21, respectively.

3.3.2 Signal Compression

It was observed that the signals may have parts either at the beginning (before the gear passes over the sensor) or at the end (after the gear leaves the sensor) not affected by aircraft loading. These parts may be disregarded to reduce the size of the signal and the amount of space required to store the signal. The first step for signal compression is to identify the lower and upper envelopes for each signal (figure 8). The envelopes are found by fitting spline functions for the signal local maxima and minima. The difference between the two envelopes is calculated at each data point. Starting from both ends of the signal, the data points are removed until the difference between the envelopes is greater than 0.5 microstrains. The point beyond which the difference becomes more than 0.5 microstrains is called the trimming point. For this particular signal, approximately 50% reduction was obtained, as presented in figure 9. Figure 9 also demonstrates omitted data points and trimming points.
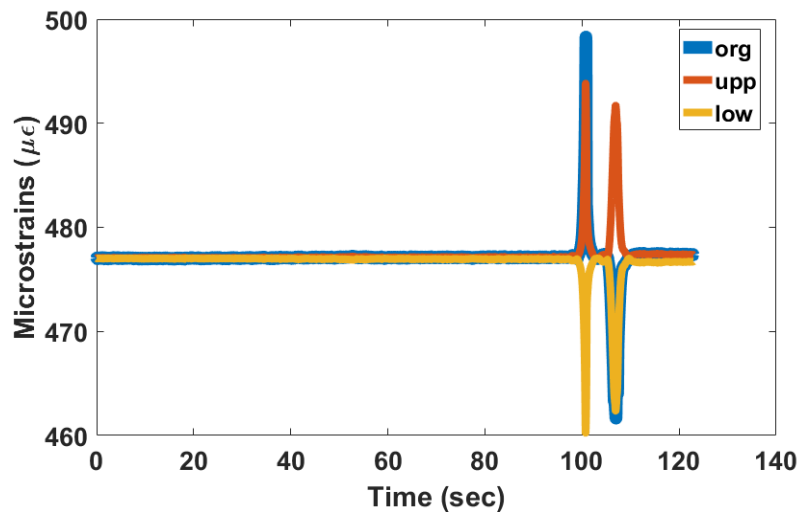

Figure 8. Upper and Lower Envelopes for a Signal

The aforementioned compression algorithm was applied to all signals. The reduction distribution is plotted in figure 9. As shown in the histogram, while some signals were reduced by 80%, some signals could not be compressed. On average, the signals were compressed by 37.8%.
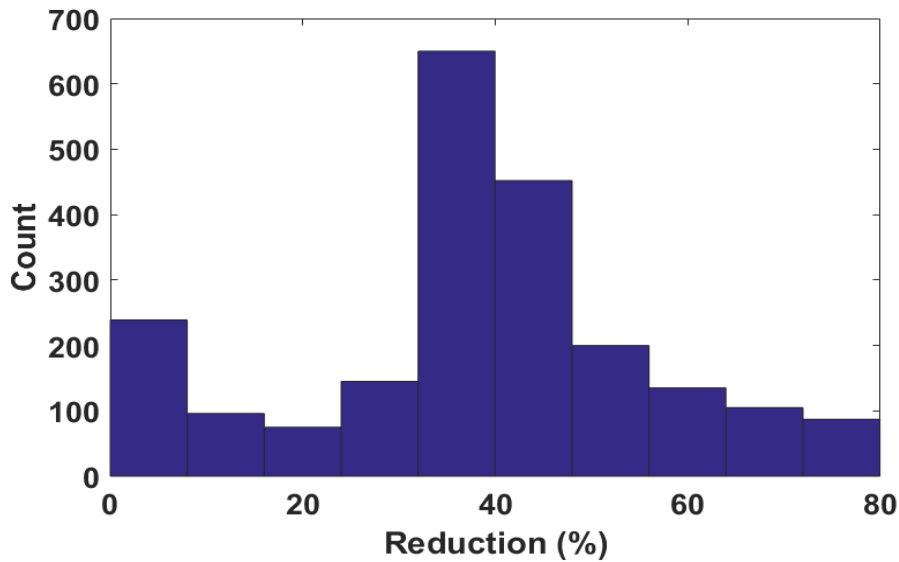
Figure 9. Signal Compression Results

3.3.3 Sensor Response Identification

The first step for extracting the response of a sensor due to gear loading is to identify the peaks of the signal. The peaks were identified utilizing a MATLAB function called "findpeaks." Spurious peaks in the signal can be eliminated by applying a threshold for the *prominence* of peaks. The prominence of the peaks can be defined as a "measure of a peak showing how much the peak stands out due to its intrinsic height and its location relative to other peaks" (MATLAB, 2016). Peaks with small prominence could represent noises in the signal and may be removed. In this study, 0.5 microstrains was selected as the threshold for the prominence.

The second step is computing a reference point, i.e., the strain measurement when the aircraft is far away from the sensor. The reference point is calculated by taking the average of the points removed in the previous step. Afterwards, the final response under the gear loading is computed as the difference between the reference point and peaks.

Figure 10 demonstrates a calculation of the response with respect to the reference points. Trimming points 1 and 2 are explained in section 3.3.2. Later, the reference points are computed by taking the mean of the points removed. If there are two reference points, as in figure 10, the average is assumed to be the final reference point. Finally, the actual response is the distance between the peak point and the final reference point. In figure 10, two responses (one tension from Peak 1 and one compression from Peak 2) were extracted as 21.22 and 15.42 microstrains, respectively. It should be noted that the number of peaks in the signal and the type of responses (e.g., tension or compression) depend on the position of the sensor with respect to the gears and the number of axles in the gears (e.g., single, tandem, or tridem). Instead of having multiple peaks as a result of multi-gear loading, the maximum response was considered to be the response from that aircraft.
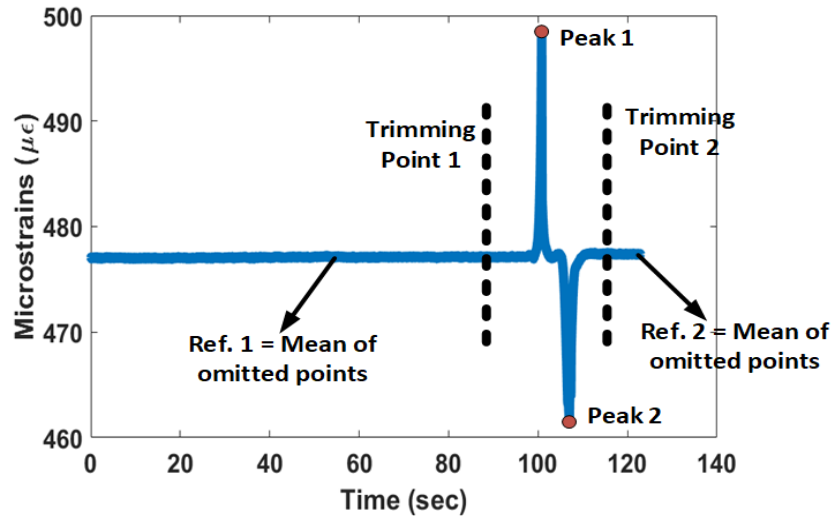
Figure 10. Peak Extraction From a Signal

3.3.4 Overall Results

Seven sensors collected data over the entire period. The signal-processing algorithm explained in section 3.3 was applied on these seven sensors to extract the maximum tensile strain at the bottom of the concrete slab for each aircraft. The results are presented in tables 4 to 10 for each sensor. In these tables, the second column (Number of Data) presents the number of data points (i.e., number of aircraft passes under which the dynamic data were collected). However, some passes did not produce any response due to deviation from the sensor location (figure 11). The number of passes with no response (NR) is given in the third column of the tables 4 through 10 (Number of NR). In some cases, data were not available, indicated by NA in the table.

Figure 11. Signal Sample With No Response

11

Table 4. Maximum Tensile Strain Measured by SG_1B

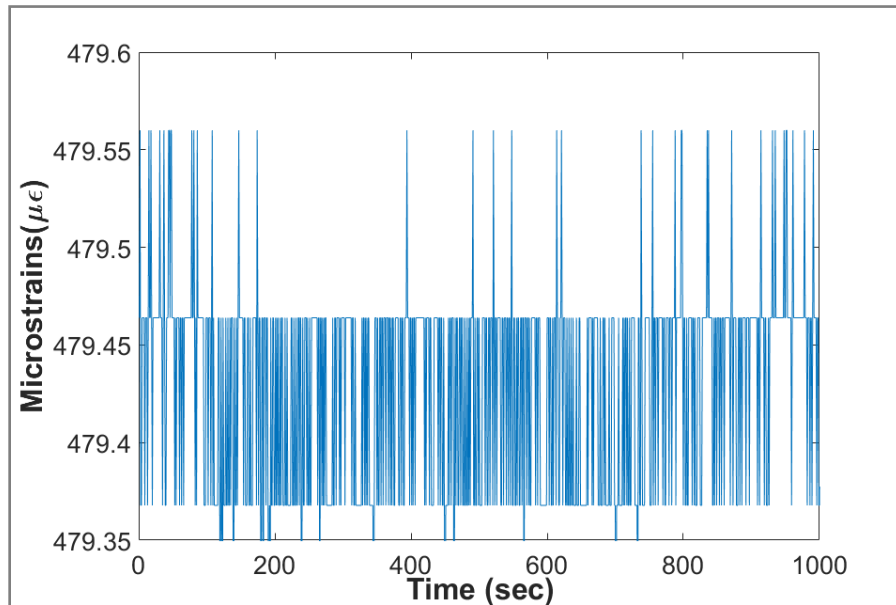| Aircraft Type	Number of Data	Number of NR	Maximum	Minimum	Mean	Standard Deviation
Boeing 777	34	3	39.88	0.96	9.26	10.31
MD 83	1	0	7.31	7.31	7.31	NA
A320	25	4	26.58	1.22	4.01	5.95
Boeing 747	20	2	40.36	1.49	18.15	12.56
Boeing 757	51	6	31.93	1.34	4.45	5.02
Boeing 737	31	7	30.62	2.12	7.52	6.73
MD-10	3	1	2.27	2.27	2.27	NA
Boeing 767	26	2	11.38	1.71	4.09	2.83
A319	5	0	4.82	1.06	2.73	1.66
A330	4	0	13.32	2.05	7.68	7.97
Embraer 190	1	0	2.90	2.90	2.90	NA
MD DC-8	1	1	NA	NA	NA	NA
A340	3	0	22.06	11.07	16.56	7.78
A380	6	0	41.46	2.32	16.57	14.70
Bombardier CRJ-900	1	0	8.24	8.24	8.24	NA
MD-88	1	0	2.51	2.51	2.51	NA
MD-11F	1	1	NA	NA	NA	NA

Table 5. Maximum Tensile Strain Measured by SG_2B

Aircraft Type	Number of Data	Number of NR	Maximum	Minimum	Mean	Standard Deviation
Boeing 777	34	5	15.65	1.45	5.57	4.02
MD 83	1	0	0.30	0.30	0.30	NA
A320	25	6	11.64	2.61	8.54	2.83
Boeing 747	20	5	12.04	0.99	5.33	3.94
Boeing 757	51	7	13.77	0.23	9.05	3.23
Boeing 737	31	6	14.61	0.35	6.17	3.79
MD-10	3	1	8.31	0.48	4.40	5.54
Boeing 767	26	3	14.11	0.55	5.75	4.10
A319	5	0	10.90	7.17	9.43	1.67
A330	4	1	10.14	10.14	10.14	NA
Embraer 190	1	0	10.47	10.47	10.47	NA
MD DC-8	1	1	NA	NA	NA	NA
A340	3	1	2.11	2.11	2.11	NA
A380	6	1	15.12	0.89	7.02	5.66
Bombardier CRJ-900	1	0	3.46	3.46	3.46	NA
MD-88	1	0	9.23	9.23	9.23	NA
MD-11F	1	1	NA	NA	NA	NA

Table 6. Maximum Tensile Strain Measured by SG_6B

Aircraft Type	Number of Data	Number of NR	Maximum	Minimum	Mean	Standard Deviation
Boeing 777	34	3	34.10	1.03	8.00	8.64
MD 83	1	0	5.59	5.59	5.59	NA
A320	25	7	5.99	0.28	2.05	1.61
Boeing 747	20	2	34.80	0.55	15.75	10.62
Boeing 757	51	7	26.89	0.95	3.95	5.09
Boeing 737	31	8	20.80	2.16	8.17	6.17
MD-10	3	1	2.06	1.01	1.53	0.74
Boeing 767	26	2	9.41	0.26	3.08	2.78
A319	5	0	3.21	3.21	3.21	NA
A330	4	0	11.23	1.12	5.17	5.34
Embraer 190	1	0	1.95	1.95	1.95	NA
MD DC-8	1	1	NA	NA	NA	NA
A340	3	0	20.46	0.66	10.49	9.90
A380	6	0	34.68	1.53	14.79	13.19
Bombardier CRJ-900	1	0	NA	NA	NA	NA
MD-88	1	0	1.64	1.64	1.64	NA
MD-11F	1	1	NA	NA	NA	NA

Table 7. Maximum Tensile Strain Measured by SG_11B

Aircraft Type	Number of Data	Number of NR	Maximum	Minimum	Mean	Standard Deviation
Boeing 777	34	3	29.98	1.46	7.70	7.04
MD 83	1	0	5.11	5.11	5.11	NA
A320	25	6	5.34	1.24	2.52	1.22
Boeing 747	20	2	29.92	1.62	14.44	9.35
Boeing 757	51	9	28.99	0.91	4.29	5.96
Boeing 737	31	6	20.73	1.25	6.27	5.29
MD-10	3	2	2.75	2.75	2.75	NA
Boeing 767	26	4	9.11	1.19	3.58	2.68
A319	5	0	2.14	1.75	1.94	0.28
A330	4	0	12.64	1.44	5.83	5.98
Embraer 190	1	0	1.72	1.72	1.72	NA
MD DC-8	1	1	NA	NA	NA	NA
A340	3	1	20.44	9.31	14.87	7.86
A380	6	1	31.22	3.87	13.69	12.25
Bombardier CRJ-900	1	0	3.25	3.25	3.25	NA
MD-88	1	0	2.34	2.34	2.34	NA
MD-11F	1	1	NA	NA	NA	NA

Table 8. Maximum Tensile Strain Measured by SG_15B

Aircraft Type	Number of Data	Number of NR	Maximum	Minimum	Mean	Standard Deviation
Boeing 777	34	4	0.25	0.12	0.18	0.09
MD 83	1	1	NA	NA	NA	NA
A320	25	7	0.25	0.21	0.23	0.03
Boeing 747	20	4	0.52	0.34	0.40	0.10
Boeing 757	51	9	0.66	0.20	0.42	0.13
Boeing 737	31	9	0.91	0.26	0.43	0.22
MD-10	3	2	NA	NA	NA	NA
Boeing 767	26	3	0.44	0.33	0.39	0.08
A319	5	0	NA	NA	NA	NA
A330	4	1	NA	NA	NA	NA
Embraer 190	1	0	NA	NA	NA	NA
MD DC-8	1	1	NA	NA	NA	NA
A340	3	1	NA	NA	NA	NA
A380	6	1	0.40	0.40	0.40	NA
Bombardier CRJ-900	1	0	NA	NA	NA	NA
MD-88	1	0	NA	NA	NA	NA
MD-11F	1	0	0.17	0.17	0.17	NA

Table 9. Maximum Tensile Strain Measured by SG_17B

Aircraft Type	Number of Data	Number of NR	Maximum	Minimum	Mean	Standard Deviation
Boeing 777	34	3	34.30	2.07	10.41	8.62
MD 83	1	0	0.48	0.48	0.48	NA
A320	25	8	25.65	0.29	13.12	7.16
Boeing 747	20	2	29.69	0.87	9.04	6.99
Boeing 757	51	7	34.02	0.33	16.40	8.67
Boeing 737	31	7	19.28	0.42	10.21	6.23
MD-10	3	2	14.19	14.19	14.19	NA
Boeing 767	26	4	30.19	1.47	14.55	8.49
A319	5	1	15.99	0.22	9.45	8.22
A330	4	0	17.42	17.42	17.42	NA
Embraer 190	1	0	21.50	21.50	21.50	NA
MD DC-8	1	0	0.98	0.98	0.98	NA
A340	3	1	NA	NA	NA	NA
A380	6	1	29.11	5.10	17.41	10.51
Bombardier CRJ-900	1	0	3.60	3.60	3.60	NA
MD-88	1	0	17.59	17.59	17.59	NA
MD-11F	1	1	NA	NA	NA	NA

Table 10. Maximum Tensile Strain Measured by SG_19B

Aircraft Type	Number of Data	Number of NR	Maximum	Minimum	Mean	Standard Deviation
Boeing 777	34	7	10.91	0.59	4.76	5.44
MD 83	1	0	0.51	0.51	0.51	NA
A320	25	7	4.92	0.20	1.23	1.65
Boeing 747	20	4	16.20	0.56	5.76	6.46
Boeing 757	51	13	9.46	0.02	1.88	2.47
Boeing 737	31	10	17.66	0.37	2.25	4.50
MD-10	3	2	NA	NA	NA	NA
Boeing 767	26	10	2.15	0.40	0.89	0.74
A319	5	1	0.75	0.40	0.58	0.25
A330	4	1	0.66	0.66	0.66	NA
Embraer 190	1	0	NA	NA	NA	NA
MD DC-8	1	0	0.08	0.08	0.08	NA
A340	3	2	NA	NA	NA	NA
A380	6	2	0.53	0.53	0.53	NA
Bombardier CRJ-900	1	0	NA	NA	NA	NA
MD-88	1	0	1.02	1.02	1.02	NA
MD-11F	1	0	0.57	0.57	0.57	NA

4. BAYESIAN CALIBRATION

After the collected data were cleaned, organized, and explored, they could be used for many purposes. In this part of the project, the data set was used for two main purposes: (1) determining the unknown material parameters using a Bayesian calibration framework; and (2) developing a machine-learning (ML) model to predict responses of airfield pavement. This section summarizes the Bayesian calibration, and section 5 explains the prediction model development.

To detect unknown material properties, an analytical model that can be assumed as an underlying function is needed. In this study, the model selected was the enhanced integrated climatic model (EICM), which is explained in detail in section 4.1. EICM can be simply defined as a function that takes material properties of a pavement and outputs a temperature profile through the depth of a pavement. It should be noted that in the calibration process, the selection of an analytical model is arbitrary. For example, a finite-element (FE) model that returns pavement structural responses could also be used. EICM was selected because of its low computation cost and numerical convenience in implementation.

After determining EICM as the analytical model, the next step was to find the input for EICM (i.e., material properties) that matched the field measurements. The search for parameters is called the *calibration process*, which is defined by Cesario and Davis (1984, p.1) as "the process of fine-tuning a model until the model simulates field conditions for a specified time horizon (such as maximum-hour conditions) to an established degree of accuracy."

Conventional calibration techniques model the calibration as a deterministic optimization problem that minimizes the residual (i.e., the difference between the output of the function and the field measurements) over the parameters. However, with the increasing interest in and appreciation of statistics, probabilistic calibration methods, such as Bayesian calibration, have been gaining popularity over the last decade. Bayesian calibration has two main advantages compared to other calibration techniques: the ability to incorporate any prior knowledge regarding the parameters to be calibrated and the ability to provide better accuracy on noisy data sets (Pavlak et al., 2013).

Because of those advantages, Bayesian calibration can be employed in various domains in engineering. For example, Wang and Sheen (2015) utilized Bayesian calibration for improving the performance of combustion kinetic simulations; Sen at al. (2017) used Bayesian calibration to estimate the source of emission in plate structures; Duputel et al. (2014) exploited a Bayesian approach for calibrating high-fidelity, deterministic earthquake simulations; and Au et al. (2003) developed a risk assessment framework under dynamic loading using Bayesian calibration. Additionally, a Bayesian approach has been used in railway engineering (Prajabat and Ray-Chaudhuri, 2017), structural health monitoring (Lam et al., 2017), and hydrological engineering (Zhang et al., 2013).

In the literature, a few software programs are suggested that implement EICM to predict temperature. ILLI-THERM (Sen and Roesler, 2018) is implementation software that is claimed to be a numerically improved version of other existing software. It requires many user-defined inputs that can be grouped into four categories: (1) numerical inputs such as number of elements and initial temperature, (2) structural inputs such as number of layers and thicknesses, (3) material properties such as thermal conductivity of concrete, and (4) climatic inputs such as hourly temperature and precipitation. The purpose of this study was to calibrate material-related input utilizing a Bayesian approach based on observational temperature data from JFK in New York. Once the calibration process is completed and unknown material properties are found, they can be used for other mechanistic models, such as FE modelling.

4.1 THE EICM AND ILLI-THERM TOOLS

EICM is a one-dimensional model that simulates heat and moisture flow within pavement structure (figure 12). The EICM, currently used in the Mechanistic-Empirical Design Guide (NCHRP, 2004) to incorporate the effects of climates and environments, has three components: a climate-materials structure (CMS) model developed at the University of Illinois; a frost-heave and settlement model developed at the U.S. Army Cold Regions and Research and Engineering Laboratory; and an infiltration drainage (ID) model developed at the Texas Transportation Institute, Texas A&M University (Zapata et al., 2007).
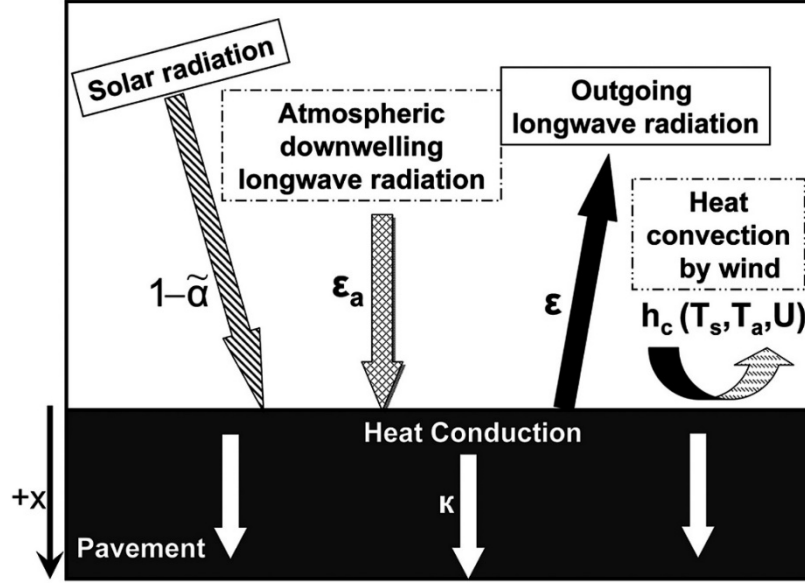
16

Figure 12. Schematic Representation of Heat-Transfer Model of Pavement (Han et al., 2011)

Since its development in 1993 (Lytton et al., 1993), the EICM has been modified a number of times (Larson and Dempsey, 1997; Witczak et al., 2000). One of the most recent improvements to EICM was by Sen and Roesler (2018), producing a software program called ILLI-THERM. ILLI-THERM essentially works on the same algorithms as EICM, except it does not consider the ID model. It can be considered a numerically improved version of the EICM. ILLI-THERM computes temperature within pavement structure by using CMS and Cold Regions and Research and Engineering Laboratory (CRREL) models, applying the boundary conditions given in equation 1.

$$Q^* + Q_F = Q_H + Q_E + \Delta Q_s \tag{1}$$

where:

Q_E is the latent heat at the surface of the pavement and equal to zero for impervious layers.
Q_F is the anthropogenic heat that is considered as zero in ILLI-THERM.
Q_H is the sensible heat flux from the pavement.
ΔQ_s is the heat stored inside the pavement.
Q^* is the incoming radiation absorbed by the pavement, calculated using equation 2.

$$Q^* = (1 - albedo) * Q_{rad} + Q_{sky} \tag{2}$$

where:

Q_{rad} is the incoming shortwave solar radiation.
Q_{sky} is the longwave radiation emitted by the sky.

4.2 BAYESIAN CALIBRATION AND MARKOV CHAIN MONTE CARLO

In Bayesian calibration, the purpose is to find the distribution of the parameter(s) conditioned on the data. This distribution is called *posterior* and is represented as follows:

$$\pi(\alpha|d) \tag{3}$$

In equation 3, α is a parameter that needs to be calibrated; d stands for the data (i.e., observation). Applying simple Bayesian rules twice, the above equation can be written as equation 4.

$$\pi(\alpha|d) = \frac{\pi(\alpha, d)}{\pi(d)} = \frac{\pi(d|\alpha)\pi(\alpha)}{\pi(d)} \tag{4}$$

In equation 4, $\pi(\alpha)$ is called *prior distribution,* which incorporates any prior knowledge about the parameter, $\pi(d|\alpha)$ is called *likelihood* and calculated based on assumed distribution, and $\pi(d)$ is called *evidence,* which is actually a normalizing constant; therefore, it is generally ignored; and *equality* in equation 4 becomes *proportionality,* as given in equation 5.

$$\pi(\alpha|d) \propto \pi(d|\alpha)\pi(\alpha) \tag{5}$$

To get a distribution for posterior (i.e., left-hand side of equation 5), a group of samples has to be generated from multiplication of prior and likelihood (i.e., right-hand side of equation 5). Because this multiplication generally does not have a closed form, a Markov chain Monte Carlo (MCMC) technique is used to generate samples.

MCMC starts with assuming a proposal distribution. Although there is no condition on selecting the proposal distribution, it is generally selected as a normal distribution. MCMC generates the samples iteratively by following the pseudocode given in algorithm 1, as shown in figure 13.

```
input: Target density (given), f(x)
Choose proposal distribution function, q(y|x)
Choose a initial accepted sample randomly, x_a
Choose a number of simulations, N
Initialize the vector for samples as 1xN, S
for i ∈ {1, 2, ..., N} do
    Draw a candidate sample from the proposal distribution conditioned on accepted
      sample, x_c ~ q(y|x_a)
    Compute acceptance rate (α)
    α = min ( 1, f(x_c)q(x_a|x_c) / f(x_a)q(x_c|x_a) )
    Draw a number from a uniform distribution between 0 and 1, u ~ U(0, 1)
    if α ≥ u then
        Accept the candidate sample
        x_a = x_c
    end
    S(i) = x_a
end
```

Figure 13. Pseudocode for MCMC

After samples are generated, posterior distribution is approximated using kernel-density estimation. Then, maximum a posteriori (MAP) estimation is conducted to find the calibrated parameter that maximizes the posterior distribution function for each input.

4.3 IMPLEMENTATION

This section presents details about implementation, along with the assumptions made. It should be noted that the scripts for the study were implemented in the MATLAB computer language.

4.3.1 Input and Prior Selection

ILLI-THERM requires material properties to predict temperature within the pavement. The number of inputs changes depending on the material type of a layer. For example, while ILLI-THERM requires 6 inputs for a concrete slab, it needs 16 inputs to proceed for base layers. Because the taxiway has 1 concrete layer supported by 2 base layers and a subgrade (soil) (figure 1), ILLI-THERM requires 54 inputs to proceed. However, based on the sensitivity analysis conducted, it was observed that material properties for the two bottom layers had negligible significant effects on temperature prediction within the concrete. Therefore, these 2 layers were omitted, and only the concrete layer at the top and the base layer underneath it were considered in the calibration process, which resulted in calibrating 22 material parameters (16 from the base layer and 6 from the concrete).

Table 11 lists all 22 material parameters used in this study. This table also shows the default values for each material parameter in the software, which can be interpreted as typical values. The priors were selected as uniform distributions bounded by 50% of the default values. For example, the prior for unit weight of concrete is a uniform distribution between 75 and 225 lb/ft³.

Table 11. All Material Parameters Used for Bayesian Calibration With Default Values

Input	Default	Input	Default
Unit Weight of Concrete (lb/ft^3)	150	Modulus of Base (psi)	32,000
Thermal Conductivity of Concrete	1.25	Saturated Permeability of Base (in./s)	313.94
Heat Capacity of Concrete $(Btu/(F*lb))$	0.28	Fredlund a of Base	7.26
Convection Coefficient $(Btu/(hr*ft*F))$	3.0	Fredlund b of Base	1.33
Emissivity	0.93	Fredlund c of Base	0.82
Absorptivity	0.7	Fredlund hr of Base	117.4
Unit Weight of Base (lb/ft^3)	127.2	Plasticity Index of Base	1.0
Thermal Conductivity of Base	0.23	D60 (mm) of Base (%)	10.82
Heat Capacity of Base $(Btu/(F*lb))$	0.17	Passing #200 of Base (%)	8.7
Porosity of Base (lb/ft^3)	0.24	Passing #4 of Base (%)	44.7
Frozen Modulus of Base (psi)	32,000	Initial Water Content of Base (ft)	15.09

4.3.2 Likelihood Selection and Computation

The selection of likelihood depends on the assumption of noise. In this study, one of the most common assumptions is followed: Noise is additive and follows a zero-mean Gaussian distribution with a known variance. In other words, the difference between the temperature data and predictions by ILLI-THERM is assumed to have a Gaussian distribution with a zero mean and known variance. Following this assumption, likelihood is computed as follows:

$$\pi(\boldsymbol{d}|\boldsymbol{\alpha}) = \frac{1}{\sigma\sqrt{2\pi}} e^{-\frac{1}{2}\left(\frac{(\boldsymbol{d}-\boldsymbol{y})-0}{\sigma}\right)^2} \tag{6}$$

In equation 6, $\boldsymbol{d}$ and $\boldsymbol{y}$ are vectors that keep temperature data (i.e., observations) and temperature predictions by ILLI-THERM, respectively. The length of the vectors is 11,808 (3 x 3,936; 3 is number of sensors, and 3,936 is number of hours of data available). In this equation, α is written in boldface because it is also a vector, whose length is 22.

In this study, it is assumed that uncertainty in the measurements is independent. Using this assumption, equation 6 for all data points can be rewritten as follows:

$$\pi(d_1, d_2, \dots | \boldsymbol{\alpha}) = \prod_{i=1}^{11808} \frac{1}{\sigma\sqrt{2\pi}} e^{-\frac{1}{2}\left(\frac{(d_i-y_i)-0}{\sigma}\right)^2} \tag{7}$$

The final step is to determine the standard deviation for the likelihood, which is generally measurement errors reported by the manufacturer of the sensors. Because the brand of the temperature sensor for the instrumentation is unknown, an online search was conducted to find reported measurement error for a similar sensor. Based on Vaisala (2017), 0.5°F was used as the standard deviation.

4.3.3 Proposal Selection and Adaptive Metropolis

Proposal distribution was assumed to be a Gaussian distribution. The mean for the proposal distribution is the last accepted sample (i.e., x_a in figure 13). However, the covariance matrix of the distribution is not known and has significant effects on the performance of the MCMC.

This study implements an adaptive Metropolis algorithm for determining the covariance matrix. This algorithm starts with the initial covariance matrix for the proposal distribution and updates it based on previous samples in the chain, based on equation 8.

$$\sigma = \frac{2.38^2}{d} Cov(x_0, x_1, \dots, x_{k-1}) + \varepsilon I_d \tag{8}$$

In equation 8, d is the dimensions of the problem, which is 22 for this study; ε is a small number that is generated using the "eps" command in MATLAB. I_d is a dxd identity matrix (22x22 for this study).

The selection of k in equation 8 determines when to update the covariance matrix. If there is one or a few samples accepted, the values in covariance become so small that it causes acceptance of highly correlated samples. To prevent this, updating of the covariance matrix is started if more than 10 samples are accepted. In this study, k was selected as 100.

4.4 RESULTS AND DISCUSSION

In this study, 10,000 MCMC simulations were conducted, resulting in 507 accepted samples (5.07% acceptance rate). Each simulation took around 30 s (approximately 3.47 days in total).

In 10,000 simulations, ILLI-THERM crashed 29 times, i.e., it did not converge and produce any results. Moreover, samples drawn from the Gaussian proposal distribution were rejected 6,348 times because they fell out of the range of uniform prior distributions. In other words, more than half the time, the samples were omitted without running ILLI-THERM. In the authors' opinion, this is not effective. Therefore, in the future, the authors suggest using, proposal distributions with bounded support in the case of having prior distributions with bounded support. Sections 4.4.1 – 4.4.3 discuss the results.

4.4.1 Convergence of MCMC

Figure 14 shows the mean and variance convergence plots for the mean of the unit weight of concrete. As shown, the chain has not yet fully converged. This observation holds for the other inputs as well. However, based on the trend (figure 14(a)), it can be said that the chain will converge for the high number of simulations.

(a)   (b)
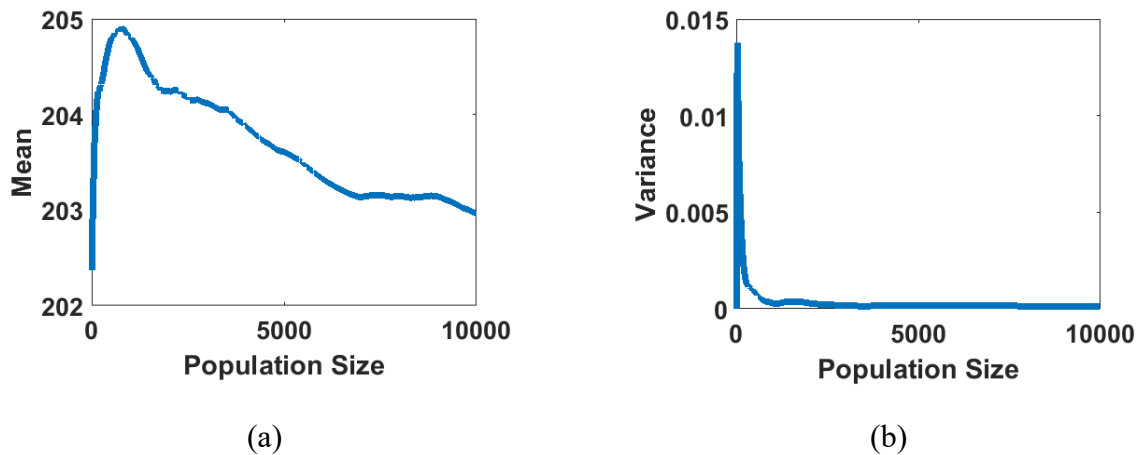
Figure 14. Mean and Variance Convergence Plots for the Mean of Unit Weight of Concrete

4.4.2 Posterior Distribution and MAP Estimation

For brevity, posterior distributions for only six concrete-related inputs (figure 15) are given in this section (the others are given appendix B). Moreover, table 12 gives the default values, MAP estimations, and percent difference between the two.

Posterior distribution showed spike-like behavior for emissivity, heat capacity, and absorptivity (figure 15). Based on this observation, it can be noted that the performance of ILLI-THERM is very sensitive to those inputs; and ILLI-THERM users should have more certain information about these inputs. For example, the difference between default values and MAP estimation for absorptivity is computed as -2.60 %.
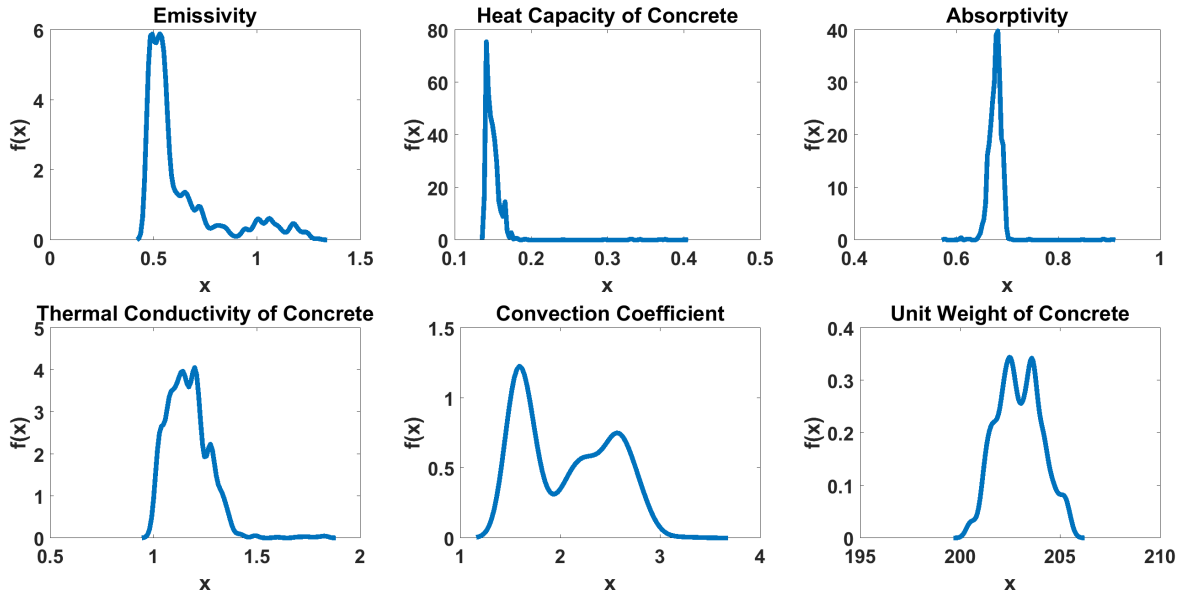
Figure 15. Posterior Distribution for Concrete-Related Inputs

Table 12. Input Values After MAP Estimation

Input Name	Default Values	MAP Estimation	Difference (%)
Unit Weight of Concrete	150	202.45	34.97
Thermal Conductivity of Concrete	1.25	1.20	-4.01
Heat Capacity of Concrete	0.28	0.14	-49.47
Unit Weight of Base	127.2	177.31	39.40
Thermal Conductivity of Base	0.23	0.33	42.95
Heat Capacity of Base	0.17	0.18	3.35
Porosity of Base	0.24	0.21	-13.13
Frozen Modulus of Base	32,000	21,707.36	-32.16
Modulus of Base	32,000	38,592.91	20.60
Saturated Permeability of Base	313.94	178.10	-43.27
Fredlund a of Base	7.26	6.22	-14.37
Fredlund b of Base	1.33	1.98	48.60
Fredlund c of Base	0.82	0.92	11.93
Fredlund hr of Base	117.4	143.30	22.06
Plasticity Index of Base	1	0.94	-6.06
D60 (mm) of Base	10.82	7.71	-28.77

Table 12. Input Values After MAP Estimation (Continued)

Input Name	Default Values	MAP Estimation	Difference (%)
Passing #200 of Base	8.7	12.49	43.56
Passing #4 of Base	44.7	22.59	-49.47
Initial Water Content of Base	15.08	12.66	-16.06
Convection Coefficient	3	1.59	-46.90
Emissivity	0.93	0.53	-42.84
Absorptivity	0.7	0.68	-2.60

4.4.3 Calibration Results

ILLI-THERM was conducted using MAP estimation to quantify the improvement due to Bayesian calibration. Figure 16 gives prediction results by ILLI-THERM before and after calibration. It is evident that Bayesian calibration improved the accuracy of ILLI-THERM by decreasing the root mean square error (RMSE) by 19 %.
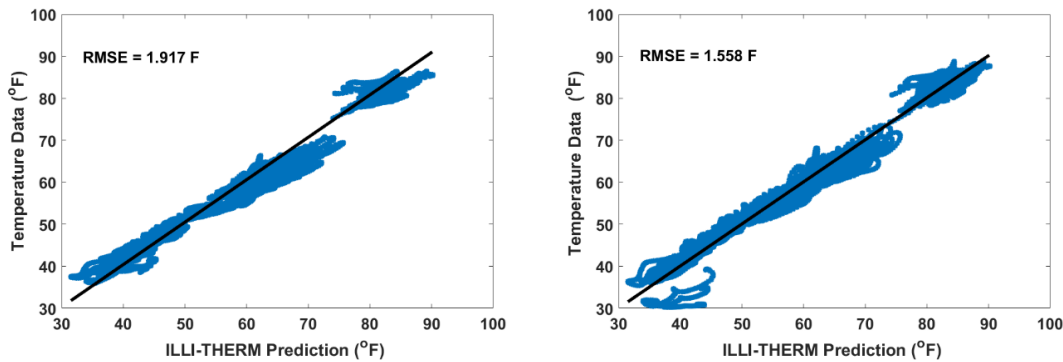
Figure 16. Calibration Results

As shown in figure 16, the calibration process increased the accuracy of temperature prediction by 19%. Additionally, it produced optimized values for unknown material properties, along with posterior distributions. The width of the posterior distributions indicated the significance of the parameters. For example, emissivity (figure 15) was found to be one of the most significant parameters due to its spike-like distribution. Furthermore, the optimized values produced can be used for various purposes. For example, they were used as input to develop a FE model (Al-Qadi & Hernandez, 2021).

5. PREDICTION MODEL DEVELOPMENT

Although the instrumentation data primarily were collected to advance understanding of pavement behavior, such comprehensive data can also be leveraged for other research objectives. For example, as previously mentioned, the data can be used to determine unknown material parameters. Another use of the data is to develop ML-based models to predict pavement responses, without having to use computationally costly, mechanistic approaches.

Accurate computation of structural responses (e.g., stress, strain, and deformation fields) plays a crucial role in the airport pavement design procedures—to predict pavement performance over the design life realistically. The state-of-the-art airport pavement design frameworks use mechanistic approaches, e.g., linear elastic theory or FE analysis, to simulate pavement behavior under aircraft loading. These approaches have to be built on assumptions that simplify or neglect variables in pavement-gear interaction that are too complicated to be represented in mechanistic equations. Although recent research findings have shown that FE analysis can be extended to include many variables omitted by conventional pavement analysis approaches, it becomes too computationally expensive to adopt in the airport pavement design frameworks.

With improvements in data storage and collection, ML is gaining momentum as a potential behavior prediction method in the field of engineering. ML may be defined as the development of algorithms that iteratively learn from data and produce reliable, repeatable decisions and results. Its ability to capture complicated relations in the data makes it a promising candidate to address challenging cases in engineering that would be difficult to solve with traditional mechanistic approaches. Additionally, unlike mechanistic approaches, it provides computational efficiency because it does not require rebuilding the model (i.e., training) every time different inputs are introduced. Therefore, ML models were developed to compute pavement responses with low computational time.

A support-vector machine (SVM) was employed to develop ML-based models to compute temperature, curling strain (due to environmental loading) within the pavement, and bending strain at the bottom of concrete slabs under Boeing 777 loading. The spacing of installed sensors allows for measurement of responses for this type of aircraft gear geometry. Although data from the Airbus A380 could be captured, the data were limited (only eight data points were available) for model development.

5.1 VARIABLE SELECTION

Before developing ML-based models, it is important to identify nonsignificant parameters and omit them to improve the performance of the learners. Several techniques are suggested in literature for selecting an optimal set of variables to minimize the total error of a regression model. This study utilizes the forward stepwise regression technique, which finds the best one-variable model that produces the highest testing accuracy. Afterward, the number of variables in the model keep increasing until a reduction in testing accuracy is observed, i.e., optimal model complexity is reached. The framework of forward stepwise regression is demonstrated in figure 17. Conventionally, linear regression is used in the stepwise regression. However, in this report, the authors use the SVM with linear kernel. The results of variable selection for temperature prediction and strain prediction are given in the sections 5.1.1 and 5.1.2.
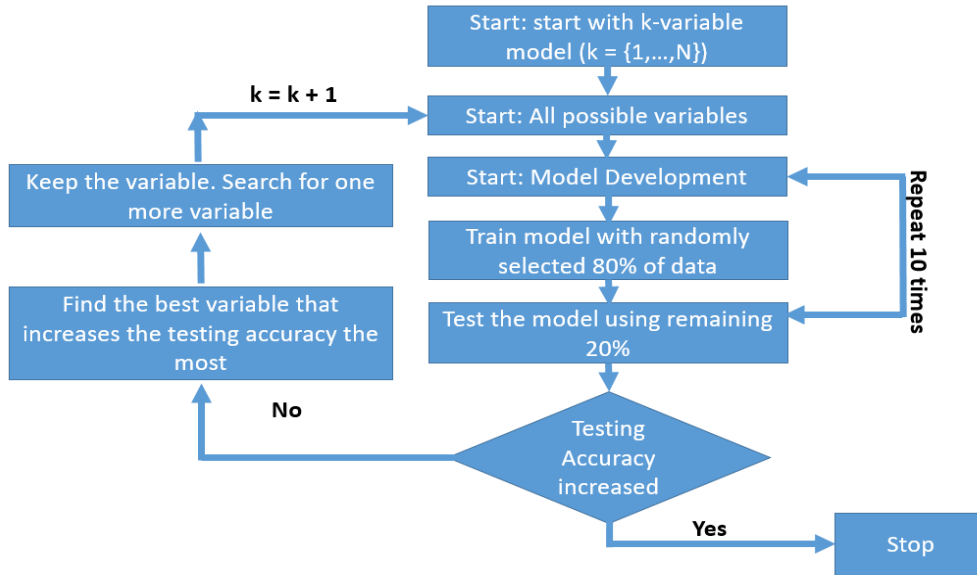
Figure 17. Framework for Forward Stepwise Regression

5.1.1 Temperature Prediction

Figure 18 shows the results of stepwise regression for temperature prediction. It can be clearly seen that the results conform to bias–variance trade-off. Although training accuracy always increases as the number of variables increases (i.e., mean square error (MSE) is decreasing), testing accuracy starts to decrease for the models with more than seven variables. The optimal variable set was found to be the air temperature, direction and speed of wind, dew-point temperature, station pressure, cloud ceiling, and maximum temperature.

As previously mentioned, the mechanistic approach used to predict temperature within pavement is called the EICM. The ML-based model developed shares six of its seven inputs with EICM. However, the station pressure, which is found to be a significant variable for temperature prediction, is not considered by EICM.
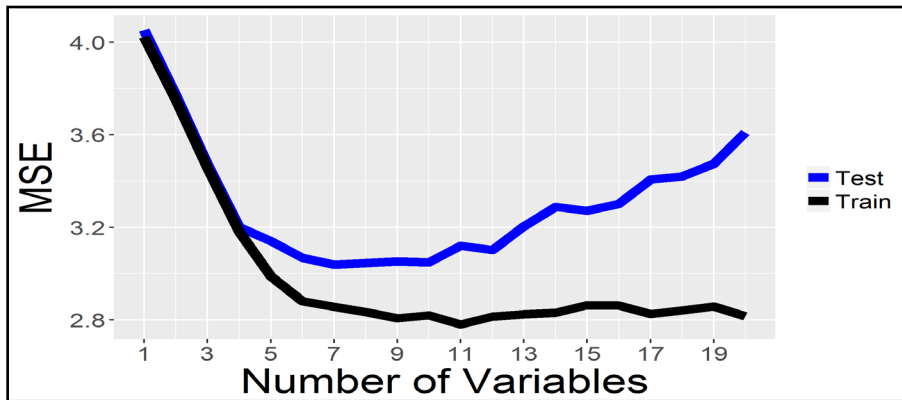
Figure 18. Variable Selection Results for Temperature Prediction

25

5.1.2 Curling-Strain Prediction

The results of variable selection for strain prediction are shown figure 19. The variable set that minimizes the total error was found to be air temperature, dew point temperature, station pressure, pavement temperature read by three thermocouples, and age of the concrete.
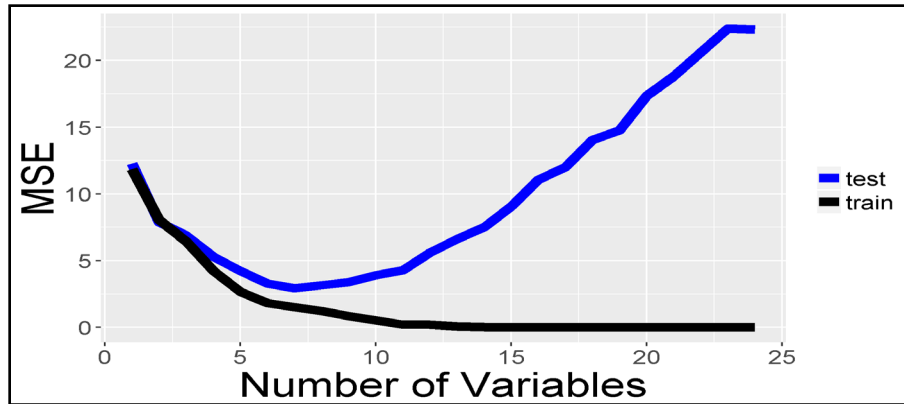
Figure 19. Variable Selection Results for Strain Prediction

Age of the concrete is the product of *feature engineering*, which can be defined as the process of using domain knowledge (of the date) to create features (variables) to improve the performance of ML algorithms. There is a clear pattern in strain measurements with respect to time as demonstrated in figure 20. Although this trend can be attributed to the creep effect of the concrete slab, other reasons may also be considered. It should be noted that age of the concrete is not considered by conventional concrete pavement design and analysis approaches; however, it appears to be a significant variable in ML-based prediction models.
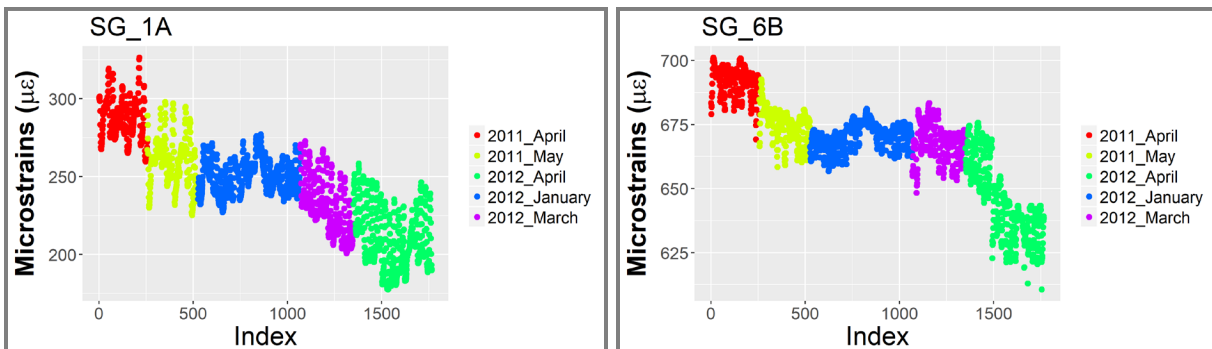
Figure 20. Demonstration of Time Effect on Strain Measurements

5.2 MODEL RESULTS

The data sets were randomly divided into three parts: training (80%), validation (10%), and testing (10%). The training dataset was used to compute SVM model parameters. Additionally, similar to the majority of ML algorithms, SVM also has the supposed hyperparameters that are essentially user inputs, such as kernel type and cost coefficient. A cross-validation step was conducted to select the hyperparameters that maximized the accuracy of the trained model in the validation

dataset. Finally, accuracy of the trained model with tuned hyperparameters is evaluated by the testing dataset.

Table 13 shows accuracy results for temperature prediction. As previously mentioned, the data are randomly split into various parts. To eliminate the effect of randomness, the splitting was done 10 times. Therefore, the results are presented with statistical measure. As shown, the MSE of the models for almost all the sensors is around 2.4°F with a coefficient of determination (R^2) value of 0.97.

Table 13. Results for Temperature Predictions

Temperature			Training		Testing	
Sensor	Depth (in.)	Statistics	R^2	MSE (F)	R^2	MSE (F)
T_1A	10	Mean	0.983	0.917	0.953	2.295
		Std	0.001	0.014	0.005	0.086
T_1B	15	Mean	0.979	0.966	0.945	2.390
		Std	0.001	0.017	0.003	0.059
T_1C	19	Mean	0.976	0.986	0.939	2.404
		Std	0.000	0.016	0.006	0.111
T_2A	10	Mean	0.984	0.874	0.955	2.276
		Std	0.000	0.002	0.004	0.102
T_2B	15	Mean	0.979	0.972	0.945	2.374
		Std	0.001	0.015	0.006	0.100
T_2C	19	Mean	0.977	0.970	0.941	2.373
		Std	0.001	0.019	0.007	0.115

Figure 21 shows the results for curling-strain prediction for various sensors (average of 10 runs) in terms of MSE and R^2, (a) and (b) respectively. The label of the sensor is given on the x-axis. As shown, MSE for the testing dataset is around a couple of microstrains; and the R^2 values are around 0.98. The strain gauges that failed after instrumentation were omitted.
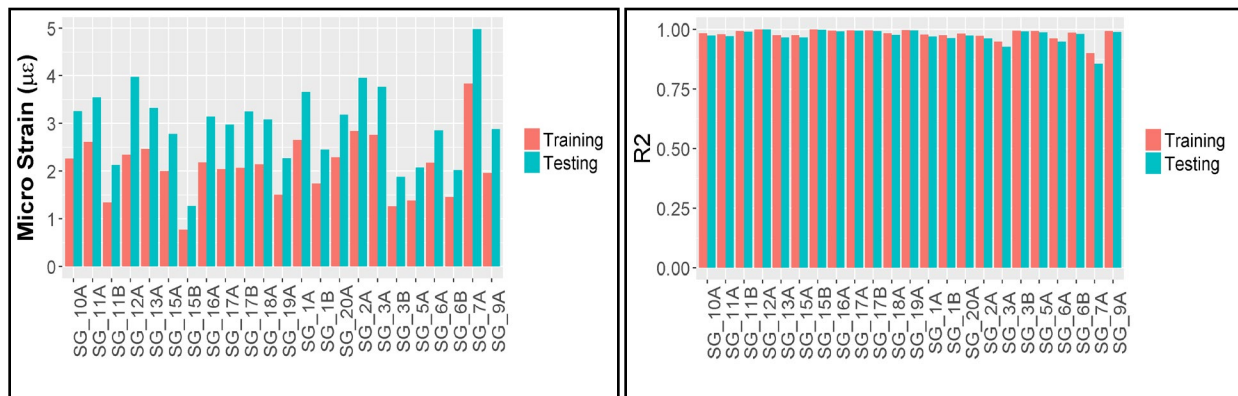
Figure 21. Strain-Prediction Results in Terms of MSE (a) and R^2 (b)

The ML-based models for the Boeing 777 were developed based on 35 data points. An important implication associated with a "small" dataset is the sensitivity of the model performance to data

splitting. In other words, performance of the models can significantly change depending on which data points the models are trained and tested on. To overcome this problem and report the true performance of models, random splitting was repeated 1,000 times.

Figure 22 presents the MSE of the prediction models (average of 1,000 runs) for Boeing 777 loading and shows that the SVM-based, ML-based models could predict the responses with an MSE range of 1.5 to 7 microstrains. The strain gauges placed at the mid-depth of the slab were not considered in the prediction models because they were close to the neutral axis of the slab, where the bending strains approach zero. Furthermore, the strain gauges that failed after instrumentation were omitted.

Two important variables are missing in the data set that might hinder the performance of the models. The first one is traffic wander, which is the lateral position of the gear with respect to sensor locations. The significance of wander on pavement responses has been highlighted by several studies, including that by Al-Qadi and Wang (2009). The second variable is speed. Although aircraft speed on the taxiway is expected to have a marginal effect on pavement responses, such information could be useful when extracting the peak response from the signal. Incorporating these two variables into data collection would improve the efficiency of ML-based models.
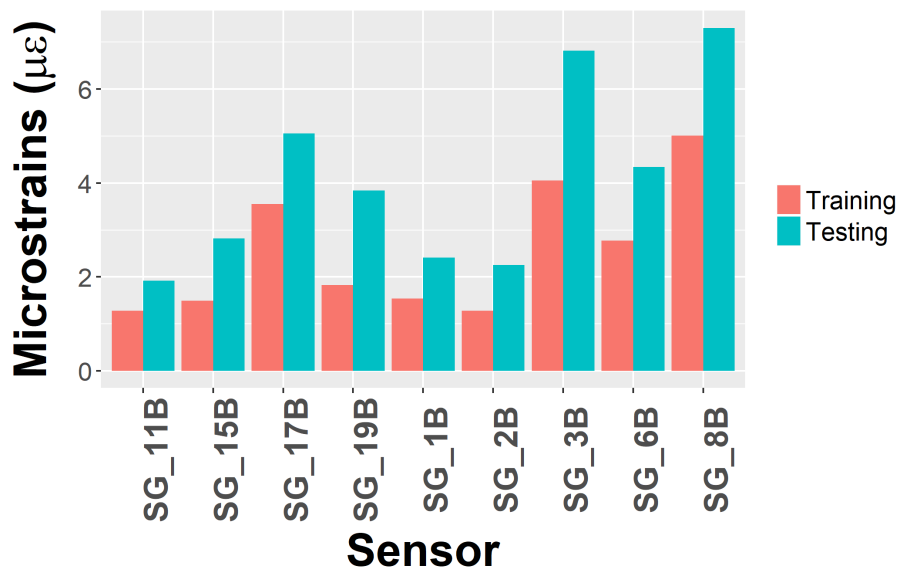
Figure 22. Prediction Results

6. SUMMARY AND CONCLUSIONS

Having an efficient airport pavement network is crucial to support growing aviation mobility and freight demands in the United States. Therefore, the FAA has conducted a number of airport pavement instrumentation projects to further advance the pavement design, analysis, and rehabilitation procedures. In one such project, four concrete slabs at a taxiway in John F. Kennedy International Airport (JFK) were instrumented to collect pavement response under aircraft and environmental loading.

This report presented the pavement data analytics for the collected sensor data. The data analytics started with the preprocessing step that transformed the data to the into Microsoft® Excel® and SQLite formats in an organized and structured way. Afterward, anomalies and outliers in the sensor data were detected and removed. The aircraft types were identified from the images taken by a camera mounted on the data-acquisition system (DAS) cabinet and added to database. Additionally, a signal-processing algorithm was developed to process and compress the signals under aircraft loading.

Two prediction models were presented in this report. The first model estimated the unknown material properties of concrete pavement slabs using Bayesian calibration framework. The calibration framework determined the material properties that matched the enhanced integrated climatic model's (EICM) temperature calculations with the field observations. The Bayesian calibration also produced the posterior distribution for each of the parameters, which can be used to infer the significance of each parameter for temperature distribution within the concrete pavement.

The second prediction model computed the pavement response using a ML algorithm called SVM. This model was developed based on the meteorological data collected at JFK. The pavement responses were predicted with a low computational time and higher accuracy. The results showed the potential, as more instrumentation data from future projects are collected, of using ML for future pavement design guidelines to incorporate various material properties and pavement structures.

In the future, the research team recommends using DOE approaches to systematize the data collection to have balanced representation of all the important variables in the database. Such a database will significantly improve the generalizability of pavement data analytics and the performance of prediction models. Additionally, the lateral position of gear loading and speed of aircrafts should be added to the database.

7. REFERENCES

Al-Qadi, I. L., & Hernandez, J. (2021). *Temperature responses of partially restrained airfield rigid pavement* [Report DOT/FAA/TC-21/31 in preparation].

Al-Qadi, I. L., & Wang, H. (2009). *Evaluation of pavement damage due to new tire designs.* Illinois Center for Transportation (ICT). No: FHWA-ICT-09-048.

Au, S. K., & Beck, J. L. (2003). Subset simulation and its application to seismic risk based on dynamic analysis. *Journal of Engineering Mechanics, 129*(8), 901–917.

Cesario, A. L., & Davis, J. O. (1984). Calibrating water system models. *Journal (American Water Works Association), 76*(7), 66–69.

Duputel, Z., Agram, P. S., Simons, M., Minson, S. E., & Beck, J. L. (2014). Accounting for prediction uncertainty when inferring subsurface fault slip. *Geophysical Journal International, 197*(1), 464–482.

Han, R., Jin, X., & Glover, C. J. (2011). Modeling pavement temperature for use in binder oxidation models and pavement performance prediction. *Journal of Materials in Civil Engineering, 23*(4), 351–359.

Lam, H. F., Hu, J., & Yang, J. H. (2017). Bayesian operational modal analysis and Markov chain Monte Carlo–based model updating of a factory building. *Engineering Structures, 132*, 314–336.

Larson, G., & Dempsey, B. J. (1997). *Enhanced integrated climatic model Version 2.0.* Department of Civil and Environmental Engineering, University of Illinois at Urbana-Champaign.

Lytton, R. L., Pufahl, D. E., Michalak, C. H., Liang, H. S., & Dempsey, B. J. (1993). *An integrated model of the climatic effects on pavements* (Federal Highway Administration Report No. FHWA-RD-90-033).

MATLAB. (2016). Prominence [Documentation] https://www.mathworks.com/help/signal/ug/prominence.html

National Cooperative Highway Research Program (NCHRP). (2004). *Guide for mechanistic-empirical design of new and rehabilitated pavement structures*. Final Report for Project 1-37A, Transportation Research Board, National Research Council, Washington, DC.

Orfanidis, S. J. (1995). *Introduction to signal processing*. Prentice-Hall, Inc.

Pavlak, G. S., Florita, A. R., Henze, G. P., & Rajagopalan, B. (2013). Comparison of traditional and Bayesian calibration techniques for gray-box modeling. *Journal of Architectural Engineering, 20*(2), Article 04013011. http://dx.doi.org/10.1061/(ASCE)AE.1943-5568.0000145

Prajapat, K., & Ray-Chaudhuri, S. (2017). Damage detection in railway truss bridges employing data sensitivity under Bayesian framework: a numerical investigation. *Shock and Vibration, 2017*, Article 6423039. https://doi.org/10.1155/2017/6423039

Sen, D., Erazo, K., & Nagarajaiah, S. (2017). Bayesian estimation of acoustic emissions source in plate structures using particle-based stochastic filtering. *Structural Control and Health Monitoring, 24*(11), Article e2005. https://doi.org/10.1002/stc.2005

Sen, S., & Roesler, J. (2018). Contextual heat island assessment for pavement preservation. *International Journal of Pavement Engineering, 19*(10), 865–873. https://doi.org/10.1080/10298436.2016.1213842

Vaisala (2017). Vaisala surface patrol pavement temperature sensor with display DSP100 series. http://www.vaisala.com/Vaisala%20Documents/Brochures%20and%20Datasheets/DSP100-Surface-Patrol-Datasheet-B210979EN-A-LOW.pdf.

Wang, H., & Sheen, D. A. (2015). Combustion kinetic model uncertainty quantification, propagation and minimization. *Progress in Energy and Combustion Science, 47*, 1–31. https://doi.org/10.1016/j.pecs.2014.10.002

Witczak, M. W., Houston, W. N., Zapata, C. E., Richter, C., Larson, G., & Walsh, K. (2000). *Improvement of the integrated climatic model for moisture content predictions*. Development of the 2002 Guide for the Development of New and Rehabilitated Pavement Structures. National Cooperative Highway Research Program (NCHRP).

Zapata, C. E., Andrei, D., Witczak, M. W., & Houston, W. N. (2007). Incorporation of environmental effects in pavement design. *Road Materials and Pavement Design, 8*(4), 667–693.

Zhang, G., Lu, D., Ye, M., Gunzburger, M. & Webster, C. (2013). An adaptive sparse-grid high-order stochastic collocation method for Bayesian inference in groundwater reactive transport modeling. *Water Resources Research. 49*(10),6871-6892. https://doi.org/10.1002/wrcr.20467
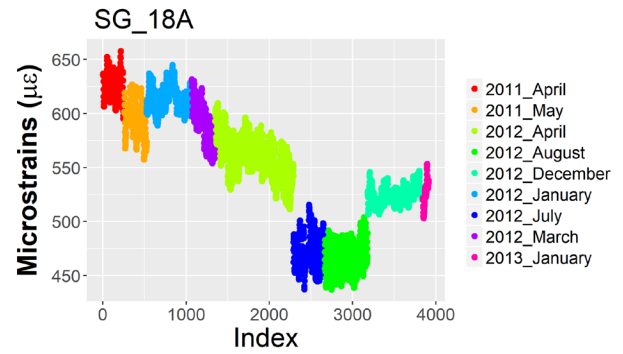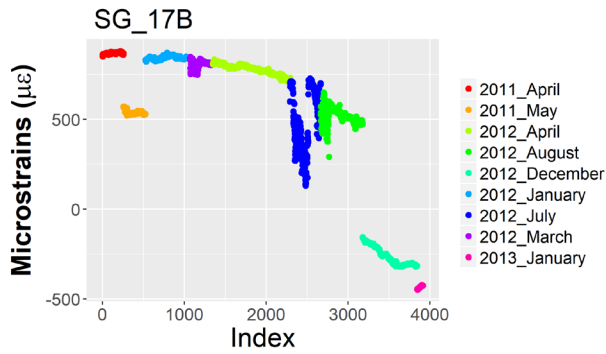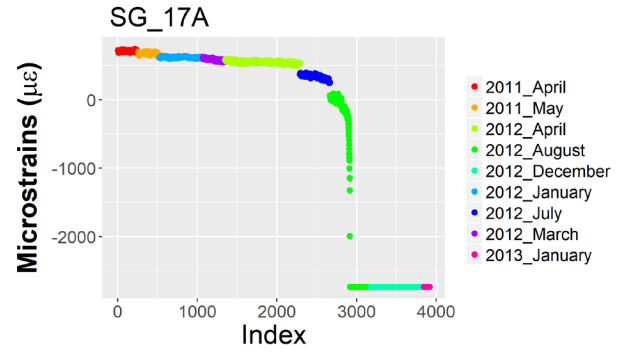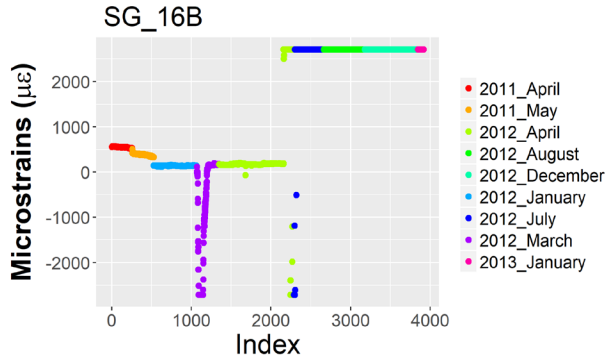
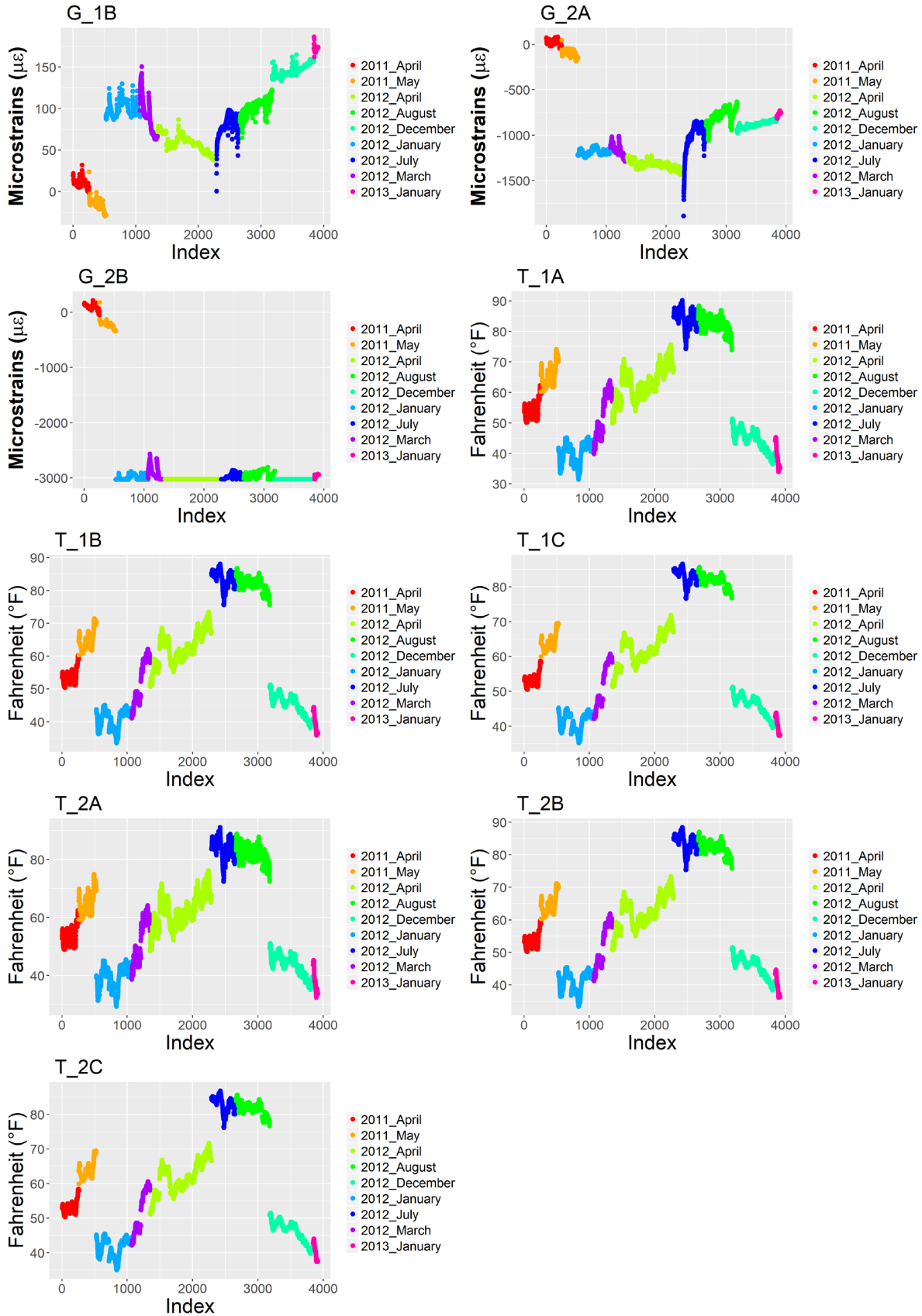## APPENDIX A—DATA PLOTS FOR ALL SENSORS

The plots in this appendix show the collected strain and temperature static data with respect to the time. The sensors that malfunctioned during the entire data collection period are not included.
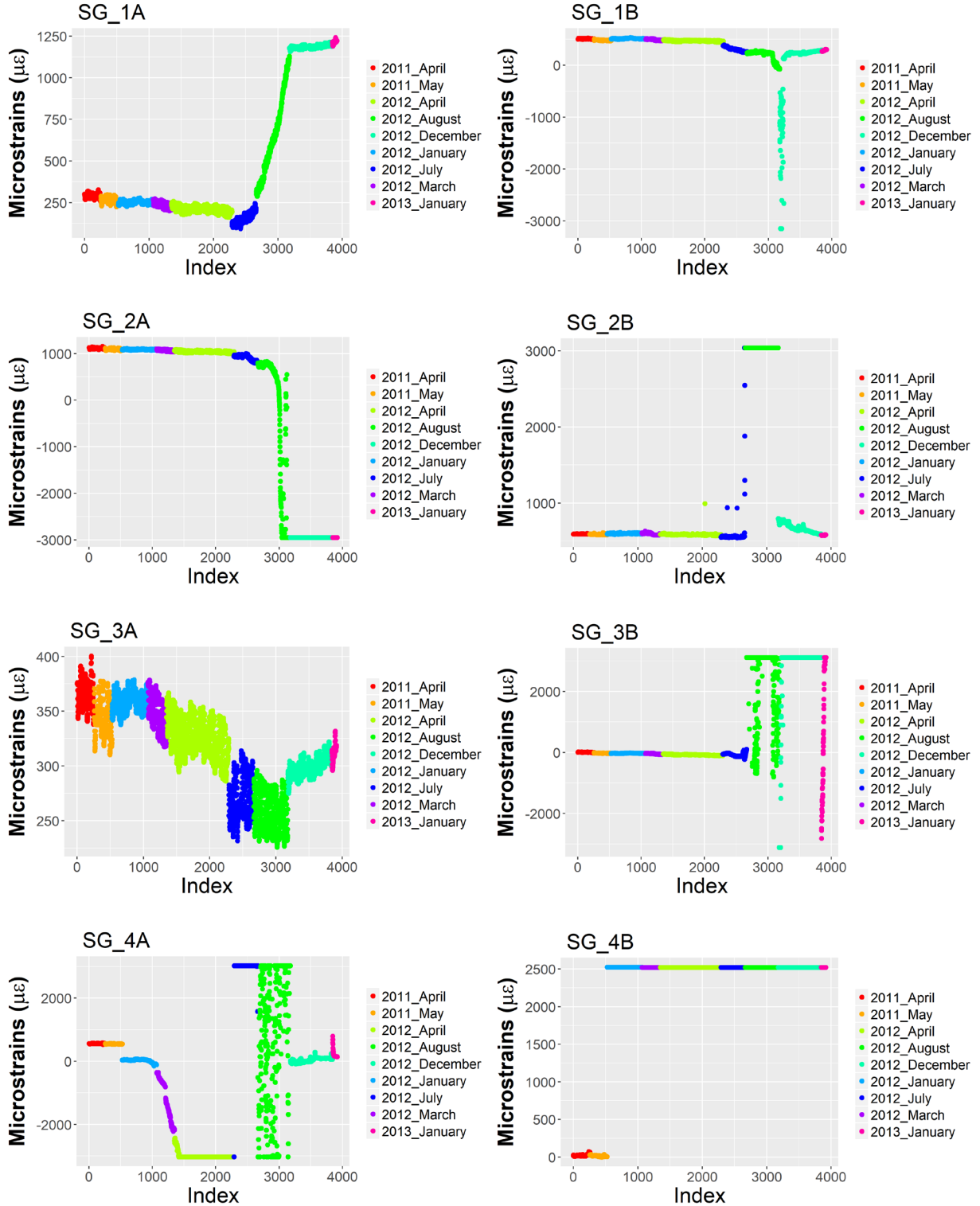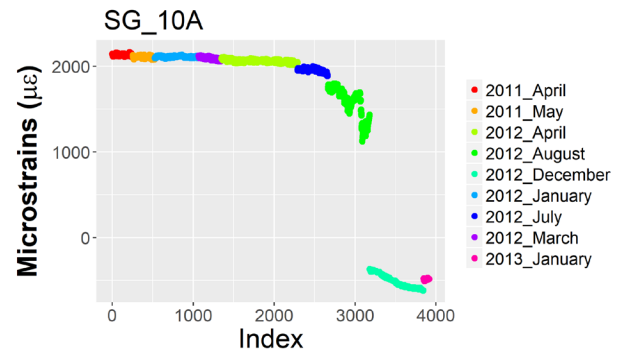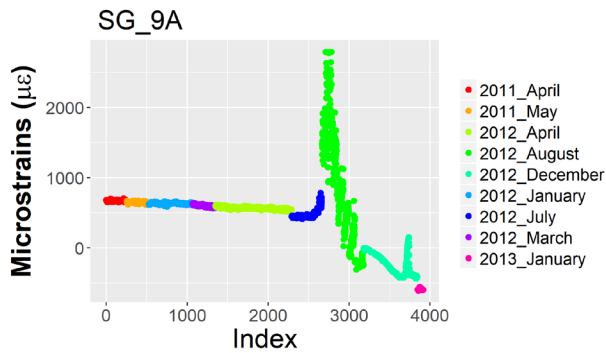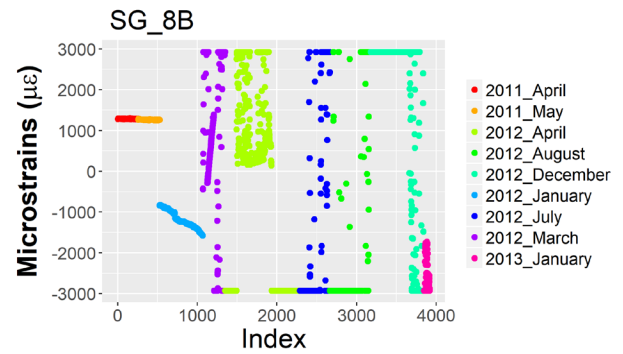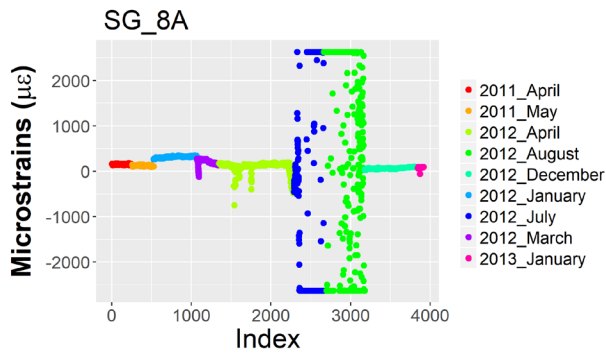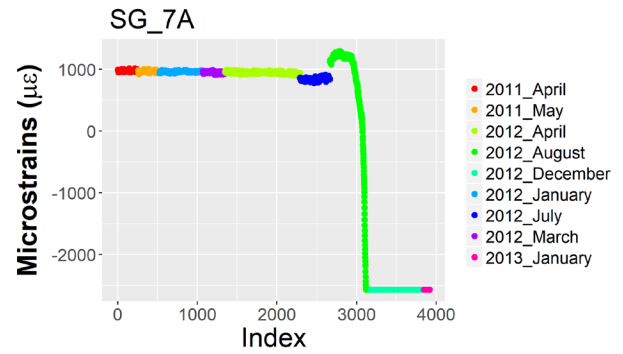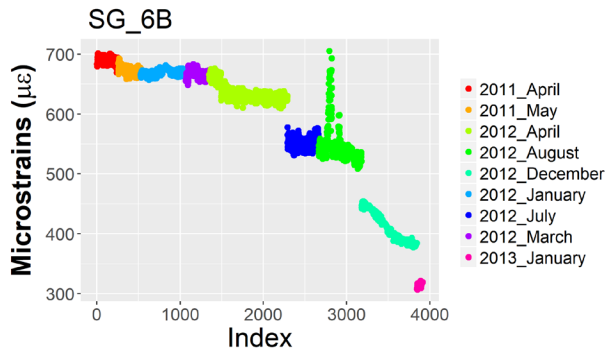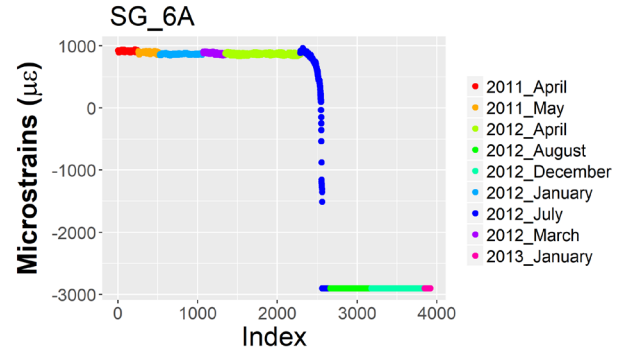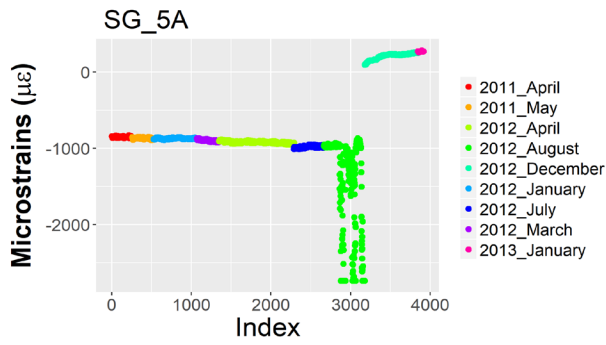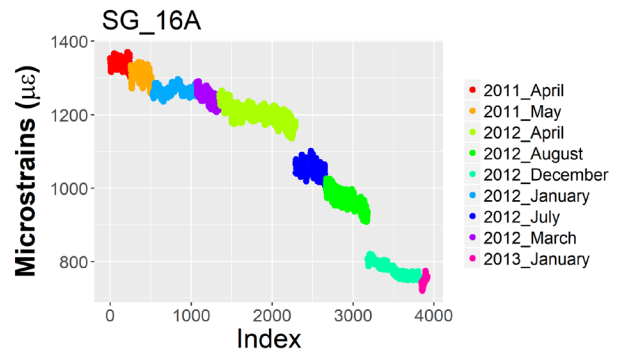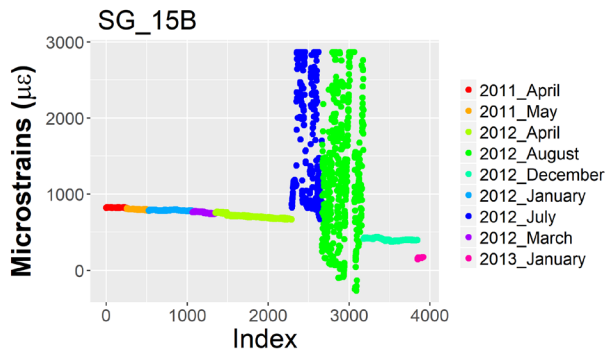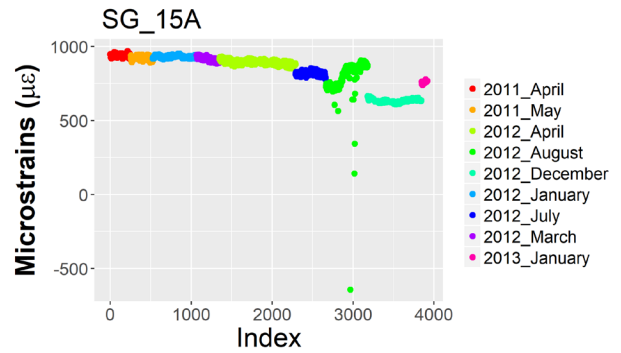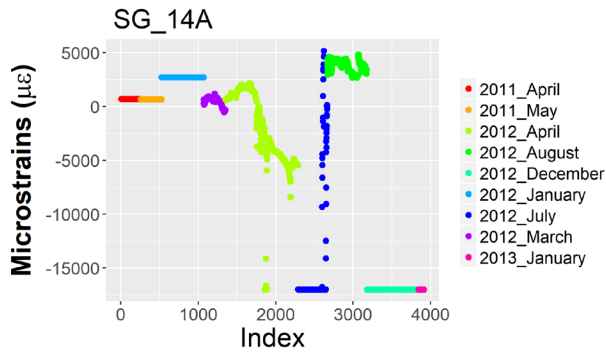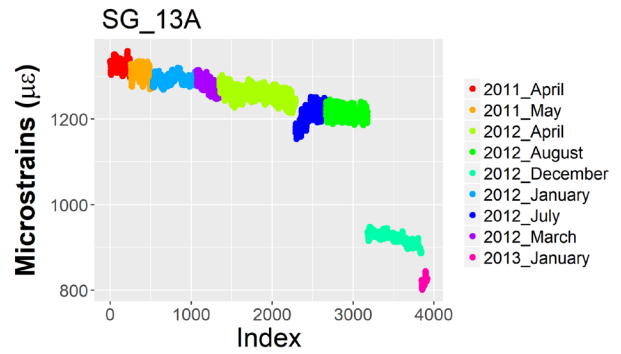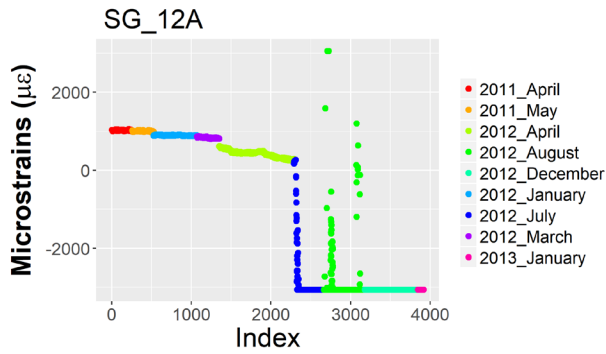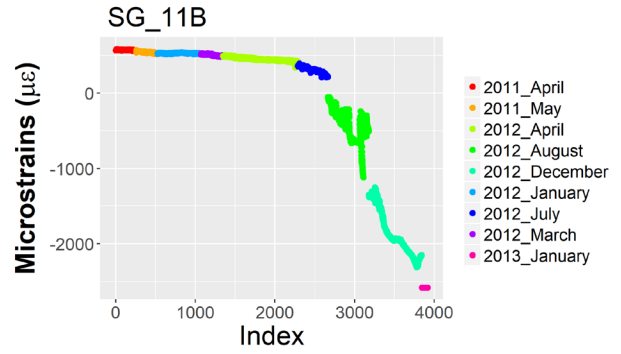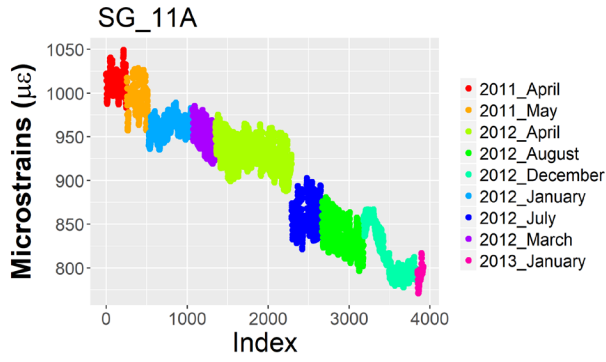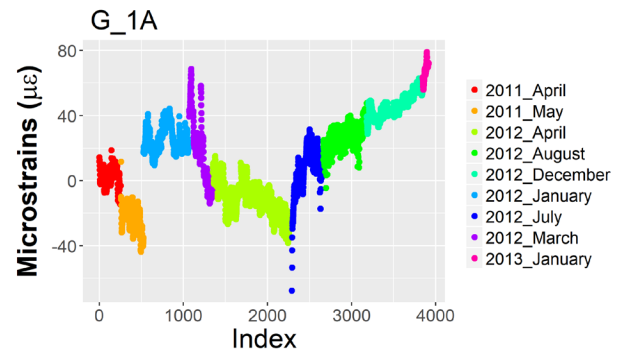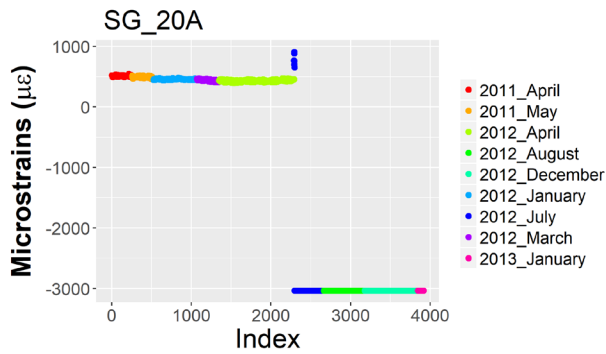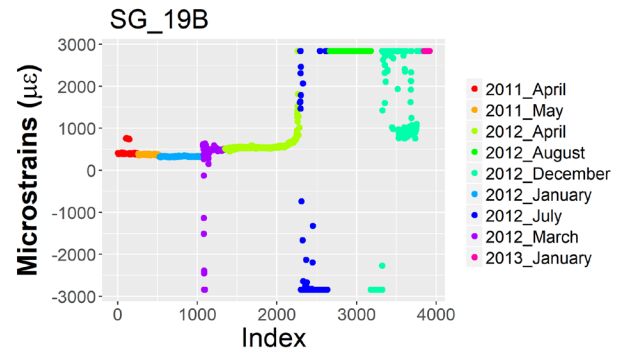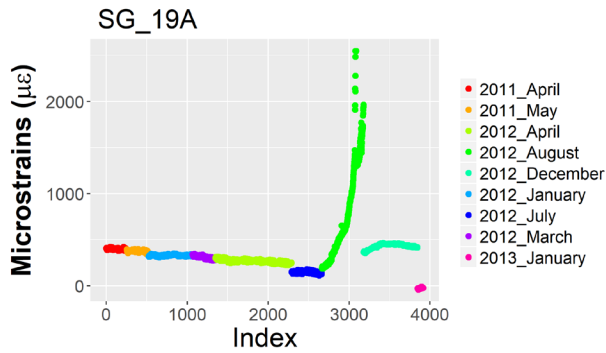
APPENDIX B—ALL POSTERIOR DISTRIBUTIONS

The plots in this appendix show the posterior distribution of the inputs of the enhanced integrated climatic model (EICM) software that were calibrated using the Bayesian calibration technique.